Ultrafast laser induced spin/electron dynamic in advanced material

Guanqi Li

MSc by research

Physics

University of York

January 2017

Abstract

I have commissioned the instrumentation of a one-colour time-resolved optical pump-probe experimental system and studied carrier dynamics in a monolayer MoSe2 sample. The system has been first tested and optimized by performing time-resolved measurements at room temperatures in an intrinsic GaAs wafer. Different modulation methods have been extensively investigated in order to increase SNR ratio. Comparing the experiment data and simulation results, double-chopping modulation is found to significantly enhance the signal-to-noise ratio. Transient reflectivity and Kerr rotation have been obtained in the GaAs test sample under various pump fluency, polarisation, and wavelength. The carrier dynamics in the GaAs sample can be reproduced and three distinct time scales have been revealed: $\tau_1 \sim 1.5\ ps, \tau_2 \sim 10\ ps, \tau_3 \sim 100\ ps$, which are consistent to what have been reported. The same experimental methods are then used to investigate the carrier dynamics of a monolayer $MoSe_2$. From the wavelength dependent transient reflectivity data, the band gap of the $MoSe_2$ sample is confirmed to be lower than 820 nm at room temperature, which is greatly reduced compared with its reported value at zero temperature. The reflectivity is found falling to negative after the initial positive peak at wavelengths longer than 790 nm. We suggest this phenomenon arise from the bound of trion and nonradioactive combination of excitons. All the reflectivity data is fitted by a bi-exponential decay function. fitting weight constants for these two dynamics have a clear dependence on laser wavelength. Transient Kerr rotation is also observed over the range of wavelength from 790 nm to 820 nm. The decay of the Kerr rotation is within the first picosecond and doesn't show an obvious wavelength dependence, which suggest an ultrafast spin relaxation time in $MoSe_2$.

Contents

List of figures

Acknowledgements

The work I have done in this thesis would not have been possible without the support of my supervisor Dr. Jing Wu and my colleagues. I have no experience in condense matter physics experiments before I began my MSc project, but with their guidance and help I finally finished commissioned the instrumentation of a one-colour time-resolved optical pump-probe experimental system.

I would especially like to say heartful thanks to my dear parents, they live in a very small town in China, and have no high education experience. They cannot understand what I am researching, but they give me unconditional support, care and love. They taught me to work hard and encourage me to carry on. I hope you know how much I love you.

Finally, I take this opportunity to say thanks to my cat, PangPang, a lovely and warmly cat. During my writing period, he was with me all the day and night. He always sleeps near my hand, and his body temperature warms my heart.

To all of you, thank you very much.

Author’s declaration

I hereby declare that this project is entirely my own work, in my own words, and that all sources used in researching it are fully acknowledged and all quotations properly identified. It has not been submitted, in whole or in part, by me or another person, for obtaining any other credit / degree. I understand the ethical implications of my research, and this work meets the requirements of the Department of Physics, University of York.

Chapter 1. Introduction

1.1 Introduction

It is well known that the electron has two intrinsic degrees of freedom (DOF), the electronic charge DOF and spin DOF. After the discovery of the electron in the end of the 19th century, the traditional semiconductor microelectronics, which uses the electronic charge DOF, had been a significant development in the 20th century. People have manipulated this electronic charge adequately and fabricated devices from nanoscale diode to Very Large Scale Integration Circuit (VLSI), which has laid the foundation of modern information world.

With the development of quantum physics and the discovery of the emission spectrum of alkali metals, the electron's spin DOF, which is called "a two-valued quantum DOF" by Pauli, was discovered. The researches of electronic spin DOF has formed a new field, namely spintronics. However, the spintronics did not attract physicists' attention until Kastler published his report about the optical pumping experimental method in 1957 [1]. The basic physical ideas and the experimental technique of today's "spintronics" came from these experiments, at the same time, a series of useful applications have emerged from these studies, such as gyroscopes and hypersensitive magnetometers [2].

As early as 1968, Georges Lampel reported the optical spin injection in semiconductor and this is a direct application of the optical transition [3], although the pumped electrons are from free conduction band, rather than valence band electrons bound by the nuclear. The discovery of the Giant magneto-resistance (GMR) based on the

electron spin DOF in 1988 [4] has generated a lot of interests among academic and industrial laboratories due to fundamental physics controlling this phenomenon and tremendous technological potential for information recording, storage and sensor industries. People are aware that the electronic spin angular momentum ($\pm\hbar/2$, here $\hbar$ is the reduced Plank constant) can be used as a carrier for information storage and transmission, and the spin DOF can be controlled by external electric field, magnetic field and optical orientation. The physical behavior of electron spin, and the associated magnetic moment, $\mu = e\hbar/2mc$, are determined by the spin interactions.

First of all, the Pauli exclusion principle, due to the eigenvalue of quantum number of the electron spin, $s = \pm 1/2$, electrons are fermions, which one state can only be occupied by no more than one electron. In fact, for now, all interactions as we known are not correspond to the Pauli exclusion principle, that is why we call it an intrinsic principle and physicists always call it an intrinsic property when they really don't know anything about it. The second is exchange interaction, which arises from the Coulomb interaction and the isomorphism of quantum particles, and it is spin-dependent due to the electron's wavefunction being subject to exchange symmetry. For fermions, it is sometimes called Pauli repulsion and thus related to the Pauli exclusion principle. Then, the spin-orbit interaction is the most important interaction among the experiments carried out in this thesis, as it is related to the optical transition rule, so it will be discussed in details in the chapter 2. The strength of spin-orbit interaction strongly increases for heavy atoms as well as outer-shell electrons. The last one is the hyperfine interaction between electron spin and nuclear spin. For GaAs

samples, as its lattice nuclei has non-zero spin, hyperfine interaction becomes quite important. For example, if the nuclei spin is 100% polarized, the effective field would be considerable strong as of several Tesla.

For the electrons in crystals, not all of them are localized around isolated atomic nucleus but some of electrons are itinerant which makes more interesting properties. A recently found DOF namely the valley DOF exists in some materials [5], and the so-called valley DOF is the extreme point of the band structure in solid materials. The theory of the valley DOF will be discussed in the chapter 2. Similar to the spin DOF, the valley DOF can be regarded as pseudospin which is potential information carriers.

So far, valley electronic materials can be classified in 2 categories. The first one includes silicon, diamond and semi-metallic elements (such as bismuth). Their Brillouin zone's valence band bottom in high symmetry axis direction is composed by an elliptical degenerate valley. While these states are occupied by electrons, an external magnetic field or translation operation can break the degenerate state. In addition, the spin-orbit coupling in these materials is relatively small compared to GaAs, so the intrinsic spin relaxation time could be very long. The internal defects of silicon or diamond can produce some quantum states with very long coherence time, therefore, they are potential candidate materials for quantum computer.

Two-dimensional (2D) atomic crystals, such as graphene and monolayer transition-metal dichalcogenides (TMDCs), have emerged as a sample to study the valley DOF in the past 10 years, in contrast to graphene, monolayer TMDCs is a non-centrosymmetric material with a direct energy gap [6]. The direct interband transition

results in an additional orbital magnetic moment at each valley, and the conservation of angular momentum makes the transition between the valence band and the conduction band following the optical select rule. In monolayer TMDCs, the valley DOF bounds with spin DOF and thus the valley DOF can be efficiently controlled by the optical helicity. Excited by the circularly polarized light, a non-equilibrium state valley current can be obtained, similar to the manipulation of the spin DOF. In order to operate the valley electronic devices, it is necessary to generate the valley-polarized current efficiently.

1.2 Experimental Techniques and Results in TMDCs

In fact, the research on valley DOF has just take advantage of a part of 2D materials' excellent properties. As physicists Andre Geim and Konstantin successfully isolated single layer graphene [5] by a simple technique, physicists suddenly found that the monolayer material has very different properties from the bulk material even made of the same atoms and structure. Although most of physicists, who had joined the 2D material quest, kept trying to find new 2D materials from the carbon family, Andras Kis focused his efforts on TMDCs. The greatest advantage of TMDCs is that TMDCs are semiconductors, which are ideal materials for electronics applications, while intrinsic graphene does not have a band gap. This direct band gap in TMDCs makes them either absorb or emit light very efficiently [7]: a single layer MoS_2 can capture more than 10% of incident photons, which is incredible for a material with only 3 monolayers thick. In a short time, TMDCs have become promising candidates for photovoltaic conversion. In 2015, Jian-Wei Pan's [8] team in China reported a new

class of single quantum emitters based on excitons that are spatially localized by defects in WSe_2 monolayers and this technology is at the heart of quantum optics and photonic quantum information technologies [8]. Even more strikingly, the underlining physical mechanism is basically the same for TMDCs MX_2 (M=Mo, W, X=S, Se) of single or couple of monolayers. The interlayer exciton relaxation in MoS_2/WS_2 has been reported in 2014, this heterostructure shows improved absorption beyond the simple superimposition of the absorptions of monolayer MoS_2 and WS_2 [9]. The result indicates that 2D heterostructures bear significant implication for the development of solar cells, photodetectors [9]. The heterostructures based on TMDCs, including BN-graphene-BN [10], single layer MoS_2 on graphene [11], and BN-TMDCs-BN, are those of the most attractive examples in the 2D materials field which have been touted by experimental physicists for potential applications, even though there is still a lot of theoretical work to do.

In order to investing the physics in TMDCs, many experimental techniques are used. As early as 1969, the experimental technique based on Hanle effect was used to investigate the spin mechanism [12]. Time-resolved Hanle measurements and time-resolved pump-probe measurements are the powerful successors. With the development of ultrafast laser source, time-resolved measurements' resolution has been significant improved. The best resolution time for time-resolved pump-probe measurements is lower than 100 fs, which help us to explore the effects within ultrashort time scales. Generally, the transient pump-probe spectrum is always fitted by multi-exponential decay function, which has serval different order time scales, and

each exponential decay corresponding to a relaxation mechanism. For example, the decay with an order of 10 picoseconds is usually related to the electron-phonon scattering [13, 14].

However, only the transient pump-probe spectrum is difficult to get the information of all channels, so other experimental techniques based on different effects characterize the spin and carrier dynamics. Generally, time-resolved photoluminance measures the exciton's relaxation through the radiative recombination in TMDCs, which has the time scale of a few picoseconds at low temperature and hundreds of picoseconds or even nanoseconds at room temperature [15-17], and these results also mutual confirmed by theoretical simulation [11, 18]. When comes to the phonon scattering, the Raman measurement is very powerful, which characterizers the phonon modes in TMDCs [19].

1.3 Scope of this thesis

The ultrafast laser induced spin and valley dynamics in 2D materials is one of the most challenging topic in recent years, with an immeasurable impact for future spintronics and valleytronics. In this chapter, we introduced the valley DOF and its great prospect in application. Chapter 2 describes the background theory of spintronics and valleytronics. Chapter 2.1 will give the valley DOF's theory explanation based on the Graphene. Then the very important spin-orbital coupling and spin-valley coupling will be considered, which attribute to the optical orientation. The optical selection rule and

many body effects that are related to the optical experiments will also be present in chapter 2.4 and chapter 2.5.

The main work for this thesis is to demonstrate how the experimental system has been established. The degenerate time-resolved pump-probe system has been built to study the TMDCs, and the laser source is a Spectra-physics Mai-Tai Ti: Sapphire oscillator. The system has been tested and optimized by intrinsic GaAs wafer, as it has been widely studied. All the experimental setup and technical details will be discussed in chapter 3. The result part will be present in chapter 4 and Chapter 4.1 focuses on the data of GaAs on the condition of various of fluency, helicity and wavelength. For $MoSe_2$ results, in chapter 4.2, the helicity-dependent and wavelength-dependent measurements are combined to carry out which means at each wavelength 3 different helicities of pumping light are applied.

Chapter 2. Background theory

2.1 Valley degree of freedom

In the past decade, 2D materials have attracted great interest because of their distinctive properties, graphene and monolayer TMDCs are the most-studied materials. They have many similarities: monolayer hexagonal structure, the layers bounded by the van der Waals' force, and the most important is that they both have the Dirac points in their energy spectrum.

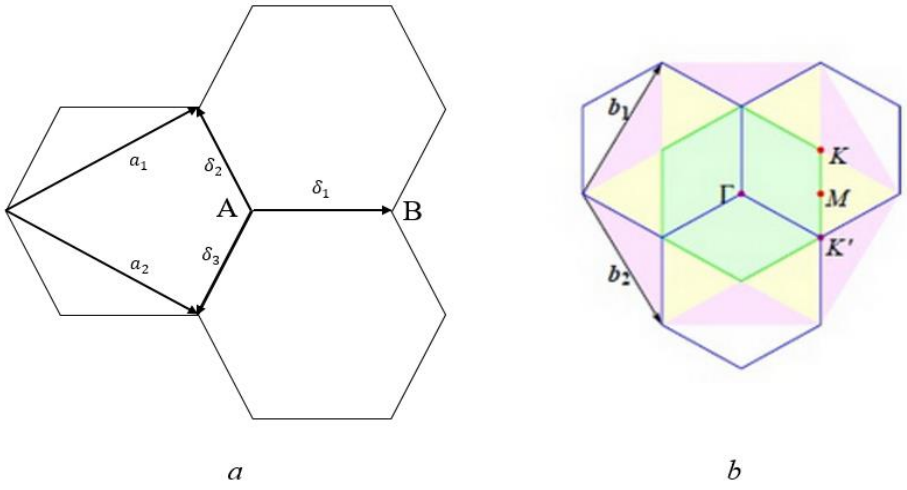

a *b*

Figure 2.1 (a) Lattice structure of graphene. A, B indicate the non-equivalent carbon atoms positions, a_i $(i = 1, 2)$ *are the lattice vectors, and* δ_i $(i = 1, 2, 3)$ *are the nearest neighbours' vectors. (b) The corresponding Brillouin zone of graphene.* b_i $(i = 1, 2)$ *are the reciprocal lattice vectors. Γ is the centre of Brillouin zone, and M is at the edge of the first Brillouin zone. Here K and* K' *are called Dirac points [20].*

Graphene is a simple model to describe the Dirac point, as it only exists two non-equivalent carbon atoms, as shown in figure 2.1 (a). When we only take the nearest and second-nearest neighbors into account, and under the tight-binding approach, the energy bands have the form:

$$E_{\pm}(k) = \pm t\sqrt{3 + f(k)} - t'f(k) \quad (2.1)$$

$$f(k) = 2\cos\left(\sqrt{3}k_y a\right) + 4\cos\left(\frac{\sqrt{3}}{2}k_y a\right)\cos\left(\frac{3}{2}k_x a\right) \quad (2.2)$$

where t is the nearest transition energy, and the plus one corresponds to the higher energy band while the minus one corresponds to the lower energy band. To comprehend the electron's properties near the Dirac points, we do an expansion in the Dirac point K. Assume that:

$$\mathrm{k} = \mathrm{K} + \mathrm{q}, |q| \ll K \quad (2.3)$$

and we can get:

$$E_{\pm}(q) \approx \pm v_F|q| + 0\{(\frac{q}{K})^2\} \quad (2.4)$$

here $v_F = 3ta/2$ is the Fermi velocity [2]. That means the Fermi velocity in graphene is independent of energy or momentum, which is different from the normal condition: $\mathrm{E(q)} = q^2/(2m)$, and more, the Fermi velocity can be compared with the velocity of light. Therefore, we need to use the Dirac equation to deal with the carriers near the Dirac points, these Dirac points in the energy spectrum look like two opposite valleys, thus we call it the valley DOF.

2.2 Spin-orbit coupling and Spin-valley coupling

2.2.1 Spin-orbit coupling in GaAs

If we take the spin into account but without spin-orbit coupling, the spin just doubles all the states, both in the conduction and valence band, and in this case the spin relaxation time will be much longer. However, the spin-orbit coupling essentially changes the energy spectrum and gives the spin more interaction mechanics to relaxation [2].

A helium atom has two electrons, and both of them have orbit angular momentums (l_1, l_2) and spin angular momentums (s_1, s_2). Six electromagnetic interactions may exist between these 4 motions: $\mathrm{G}_1(s_1, s_2)$, $\mathrm{G}_2(l_1, l_2)$, $G_3(l_1, s_1)$, $G_4(l_2, s_2)$, $G_5(l_1, s_2)$, $G_6(l_2, s_1)$, since $G_5(l_1, s_2)$ and $G_6(l_2, s_1)$ are extremely weak, they can be ignored. Consider two cases, first is that $\mathrm{G}_1(s_1, s_2)$ and $\mathrm{G}_2(l_1, l_2)$ are predominant interactions, which means these two electrons spin motions have strong interaction, and their orbital motion have strong interaction. Second, $\mathrm{G}_3(l_1, s_2)$ and $\mathrm{G}_4(l_2, s_1)$ are in the dominant position, which means these interactions are induced by each electron. Generally, as heavy elements have larger nuclear charge, the electromagnetic interaction between electrons and nuclear is stronger, and for outer electron, there is a certain probability for them to approach the unscreened nucleus, so the heavy elements' outer shell electrons have a strong spin-orbit coupling. Because of this, neither the spin angular momentum nor the orbital angular momentum is no longer conserved, but total angular momentums $J_1 = s_1 + l_1$, and $J_2 = s_2 + l_2$.

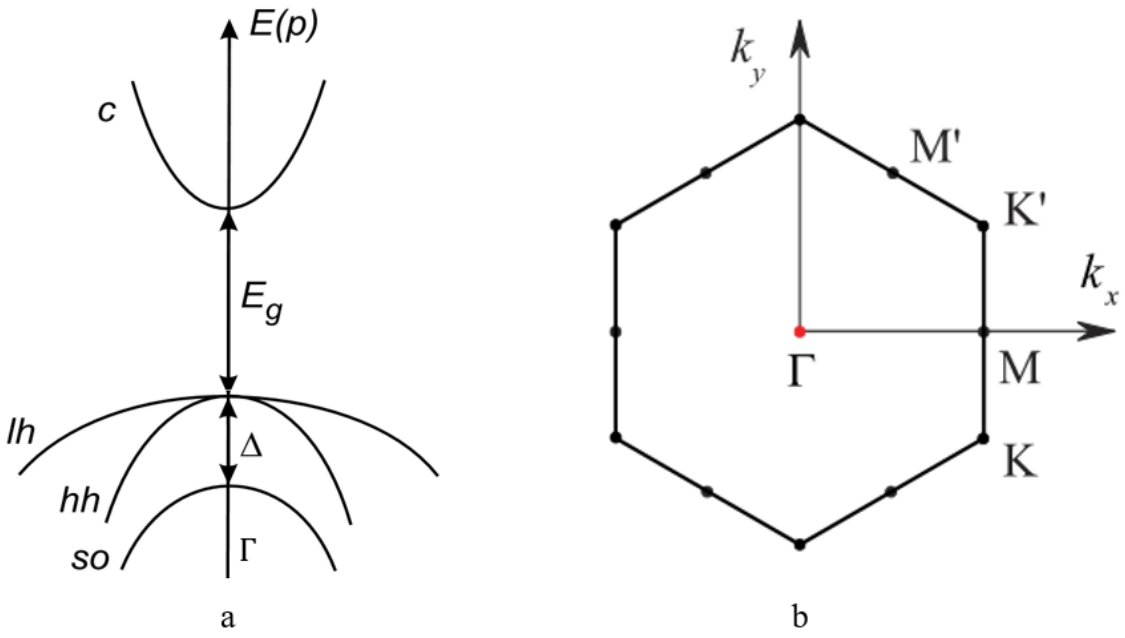

Figure 2.2 (a) Band structure of GaAs near the centre of the Brillouin zone $p = 0$. E_g: band gap energy; c: conduction band; hh: heavy hole band; lh: light hole band; so: split-off band [2]. (b) Brillouin zone of the monolayer $MoSe_2$.

Now we consider the change of band structure, the total angular momentum still follows the quantized angular momentum rule, and the eigenvalues of j^2 are $j(j+1)$ with $|l-s| \leq j \leq |l+s|$. Therefore, the $l = 0$ state (bottom of conduction band) is not affected ($j = s = 1/2$), however, the $l = 1$ state is split into two states (top of valence band) with $j = 3/2$ and j $= 1/2$.

For GaAs, the transition point is in the center of Brillouin zone, as shown in the figure 2.2a, where the electron's quasi-momentum $q = 0$, so we must have a four-fold degenerate state ($j = 3/2, J_z = +3/2, +1/2, -1/2, -3/2$), and a doubly degenerate states ($j = 1/2, J_z = +1/2, -1/2$) [2]. The energy distance Δ between the ($j = 3/2$) state and the ($j = 1/2$) state is called the spin-orbit splitting, as we

mentioned before, for semiconductors composed of heavy elements, the value of Δ could be quite large, like GaAs, $\Delta = 0.34$ eV.

2.2.2 Spin-valley coupling in TMDCs

TMDCs had been studied in bulk form since the 1960s, the structure is shown in figure 2.3a, which has an inversion centre. As it has no spontaneous magnetic field, the time-reversal $E^{\uparrow}(k) = E^{\downarrow}(-k)$ is valid, here $\uparrow$ ($\downarrow$) indicates the spin state, and k is the electron's momentum wavenumber vector. When we combine the time-reversal with the inversion symmetry $E^{\uparrow}(k) = E^{\uparrow}(-k)$ the spin degeneracy $E^{\uparrow}(k) = E^{\downarrow}(k)$ is established in the TMDCs bulk. However, when it is thinned down to a monolayer, the inversion symmetry will be broken, a spin splitting is expected. Turning to the spin-orbit coupling, the spin-orbit coupling breaks the spin degeneracy of the valence band, and the splitting energy increases with the momentum increases, and the fully relativistic first-principles calculation gives the result of 0.18 eV at the K and K$'$ points [21].

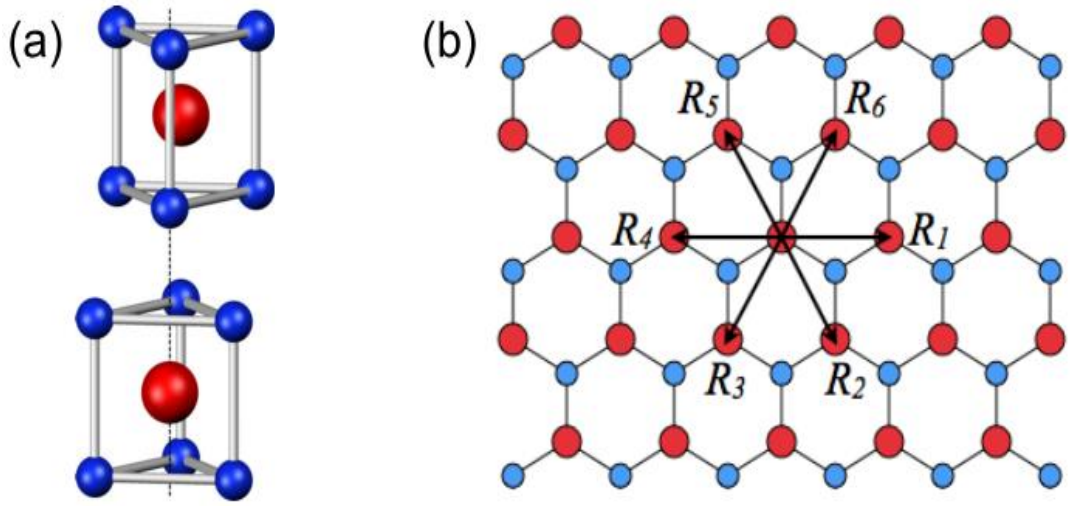

Figure 2.3 (a) The unit cell of bulk 2H-TMDCs, which has the inversion centre located in the middle plane. It contains two unit cells of TMDCs monolayers, which lacks an inversion centre. (b) Top view of the TMDCs monolayer. R_i are the vectors connecting nearest Mo (W) atoms [22].

The monolayer $MoSe_2$ are direct-band-gap semiconductors with the valence-band maximum (VBM) and conduction-band minimum (CBM) at the K point of the Brillouin zone, schematically shown in figure 2.3b. The band structure of $MoSe_2$, consists of partially filled Mo *d*-bands lying between Mo-Se s-p bonding and anti-banding bands [22]. The reflection symmetry in the *z* direction permits hybridization between the (d_{z^2}) orbital and (d_{xy}, d_{yz}) orbitals, which open a band gap at the K and K' points. For the monolayer $MoSe_2$, the band gap is about 1.56 eV (790 nm) [22].

2.3 Spin relaxation

Spin relaxation mechanisms are at the heart of all spin phenomena. All spin relaxation can be regard as the effect of a time-dependent effective magnetic field. There are 4 kinds of spin relaxation mechanisms: Elliot-Yafet (E-Y) mechanism, Dyakonov-Perel (D-P) mechanism, Bir-Aronov-Pikus (B-A-P) mechanism, and hyperfine interaction relaxation. E-Y mechanism and D-P mechanism originate from spin-orbit coupling. As all TMDC materials have the strong spin-orbit coupling, the E-Y and the D-P mechanism are deeply studied. The significant difference between these two mechanisms are: The E-Y mechanism applies to spin-orbit coupling system with inversion symmetry, the spin rotates during the electrons collisions, and $1/\tau_s \sim 1/\tau_p$; while the D-P mechanism applies to spin-orbit coupling system without inversion symmetry, the spin rotates between the electrons collisions, and $1/\tau_s \sim \tau_p$ [23].

B-A-P mechanism is caused by the exchange interaction between the conduction band electron and all valence band electrons spins, which is a mechanism of the spin relaxation of non-equilibrium electrons in *p*-type semiconductors. Hyperfine interaction relaxation is usually in a disordered state, due to the extremely weak corresponding relaxation rate. However, if the lattice nuclei spins have a high spin polarization rate, the nuclei would not only provide random effective magnetic fields, in that case, hyperfine interaction relaxation should be taken into consider.

2.4 The optical select rule

The electron can transit from the valence band to the conduction band by absorbing a photon, and this process must keep to the principle of conservation of energy, momentum, and angular momentum. For a single photon, the energy is:

$$\mathrm{E} = hc/\lambda \quad (2.10)$$

where h is the Planck constant, c is the velocity of light and λ is the wavelength of light. The conservation of energy requires that the single photon's energy must be equal or greater than the bandgap energy. The momentum of photon can be ignored when it compares with the momentum of electron, hence in direct transition the electron does not change its momentum, while in indirect transition the electron must absorb a phonon to change its momentum. Unlike the photon's momentum can be ignored, the photon has the angular momentum of $-\hbar$ or $\hbar$, which correspond to left-handed (σ^-) and right-handed (σ^+) light respectively, and the linear polarized light is regarded as a combination of left- and right-handed circular polarized light.

Figure 2.4a schematic the band structure of intrinsic GaAs and related interband transition, and the Bloch states are denoted by the total angular momentum's projection onto the Z axis. According to the effective mass, the $|3/2, 3/2\rangle$ and $|3/2, -3/2\rangle$ states are called heavy hole (HH), while the $|3/2, 1/2\rangle$ and $|3/2, -1/2\rangle$ states are called light hole (LH), but in the center of Brillouin zone their energy is degeneracy. Since GaAs is a direct semiconductor, there is no phonon participate in the transition. In our experiments, the regulate range of the laser is from 760 nm to

875 nm, so the laser cannot excite the $|1/2, 1/2\rangle$ and $|1/2, -1/2\rangle$ states, so we take no account of this states.

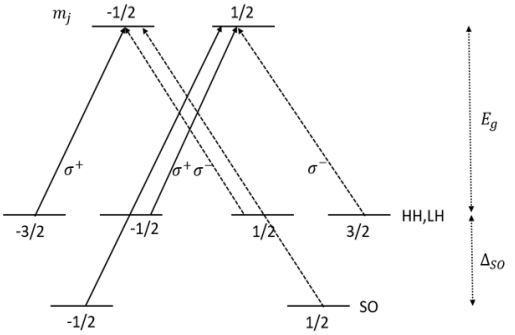

(a)

Symmetry	$\|J,m_j\rangle$	Wave function
Γ_6	$\|1/2,1/2\rangle$	$\|S\uparrow\rangle$
	$\|1/2,-1/2\rangle$	$\|S\downarrow\rangle$
Γ_7	$\|1/2,1/2\rangle$	$\|-(1/3)^{1/2}[(X+iY)\downarrow-Z\uparrow]\rangle$
	$\|1/2,-1/2\rangle$	$\|(1/3)^{1/2}[(X-iY)\uparrow+Z\downarrow]\rangle$
Γ_8	$\|3/2,3/2\rangle$	$\|(1/2)^{1/2}(X+iY)\uparrow\rangle$
	$\|3/2,1/2\rangle$	$\|(1/6)^{1/2}[(X+iY)\downarrow+2Z\uparrow]\rangle$
	$\|3/2,-1/2\rangle$	$\|-(1/6)^{1/2}[(X-iY)\uparrow-2Z\downarrow]\rangle$
	$\|3/2,-3/2\rangle$	$\|(1/2)^{1/2}(X-iY)\downarrow\rangle$

(b)

Figure 2.4 (a) Schematic interband transition in GaAs. The band gap E_g in the centre of the Brillouin zone is approximately 1.52 eV (transition photon wavelength: 811 nm) in 0 K, and the value of the spin split-off energy $\Delta_{SO}= 0.34$ eV (transition photon wavelength: 700 nm) in room temperature. (b) Angular and spin part of the wave function in the centre of the Brillouin zone [23].

An incident σ^+ (σ^-) photon with the energy a little over than band gap will be absorbed by the $|3/2, -3/2\rangle$ ($|3/2, 3/2\rangle$) and $|3/2, -1/2\rangle$ ($|3/2, 1/2\rangle$) states, these electrons will transmit to the conduct band and holes will be left in the valence band. Generally, the excitation electron and the hole will be attracted to each other, this bound state is called an exciton. However, the transition probability is different, it follows from the Table in Figure 2.4b that:

$$\frac{P_{HH}}{P_{LH}} = 3 \quad (2.11)$$

The spin polarization is defined as:

$$P_n = (n_+ - n_-)/(n_+ + n_-) \quad (2.12)$$

here n_+ $(-n_-)$ is the density of electrons with spin up (down). Therefore, a right-handed light will inject a spin polarization:

$$P_n = (3 - 1)/(3 + 1) = 1/2 \quad (2.13)$$

So, this method is called optical spin orientation.

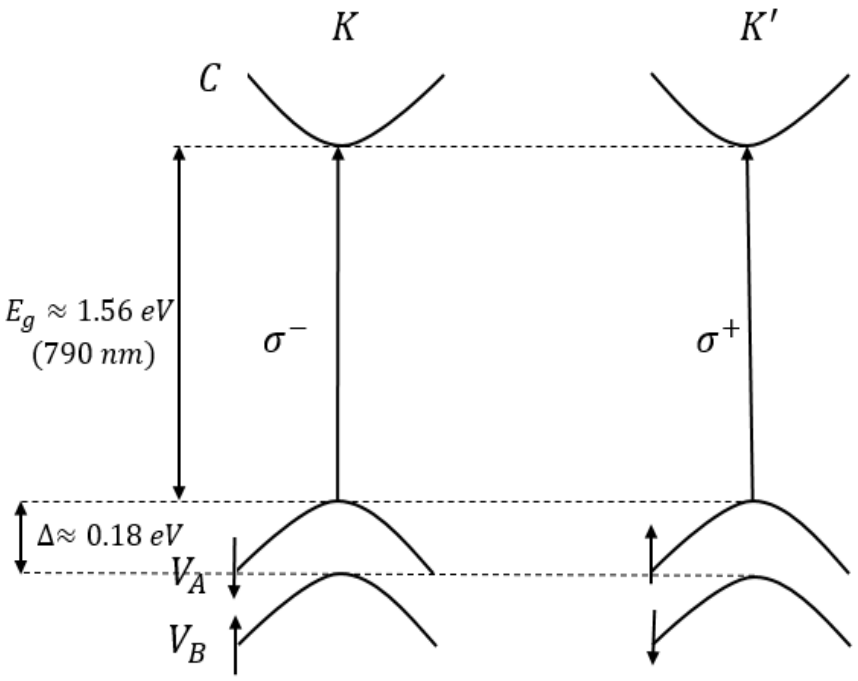

Figure 2.5 Optical transition in monolayer $MoSe_2$. K (K') is the valley index; C indicates the conduction band; V_A is the top of valence band, while V_B is the spin-splitting band; ↑ (↓) *indicates the spin state.*

The spin polarization in monolayer TMDCs can be 100%, due to the giant spin-orbit coupling induced spin splitting and the spin-valley coupling. Figure 2.5 depicts the

interband optical transition from valence band to conduction band at the *K* and *K'* valley of monolayer $MoSe_2$. In the *K* valley, the z-component of the total angular momentum of valence band are:

$$m_{j,A} = -1/2\,, \quad m_{j,B} = 1/2 \quad (2.14)$$

And for the bottom of conduction band:

$$m_{j,C1} = -1/2, \quad m_{j,C2} = -3/2 \quad (2.15)$$

These two states are degenerate at the *K* valley. Due to the conservation of angular momentum in z-axis, the interband transition only exists 2 pathways: $m_{j,A} \rightarrow m_{j,C2}$ by absorbing a left-handed photon, or $m_{j,B} \rightarrow m_{j,C1}$ by absorbing a right-handed photon. However, the latter photon's energy is 0.18 eV higher than the former. Therefore, when a left or right-handed light with photon energy equals to the bandgap energy is used for optical spin orientation, in the ideal situation, 100 % spin polarization can be obtained in monolayer TMDCs.

2.5 Many-body effects

Monolayer TMDCs exhibits strong many-body effects mediated by Coulomb interactions, since the Coulomb interactions in 2D materials is greatly enhanced due to reduced dielectric screening in gapped 2D crystals and the relatively heavy carrier band masses associated with the Mo d-manifolds [5]. A manifestation of these many-body interactions is the formation of excitons, trions, and even biexciton, bound 2 excitons.

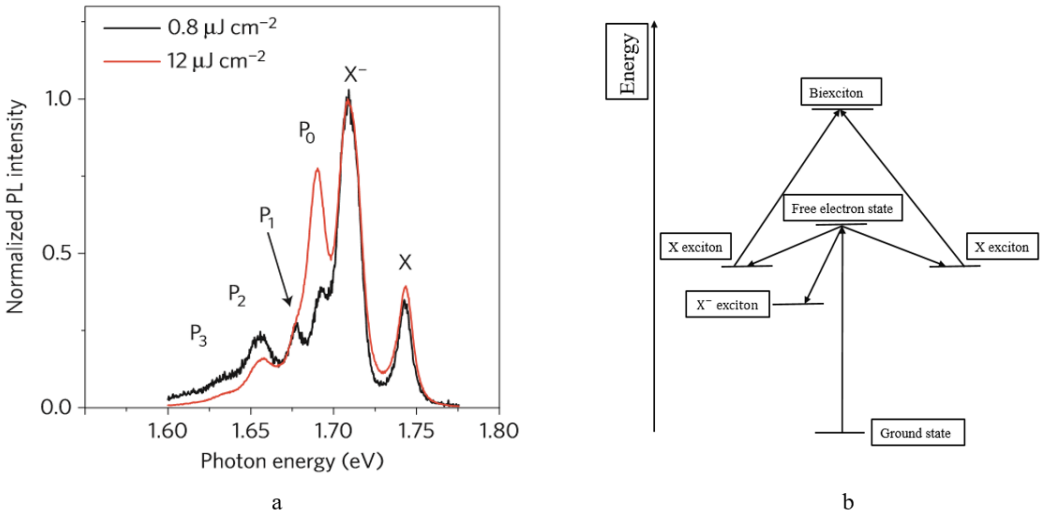

Figure 2.6 (a) Monolayer WSe_2 photoluminescence spectra at 50 K under ultrafast pump radiation at different fluencies. The peak at 1.71 eV arises from emission from neutral exciton (X), the peak at 1.71 eV from negative trions (X^-), and the peak P_0 at 1.68 eV from the biexciton P_0, which grows linearly with fluency [24]. (b) The bound states pathway and their energy.

Figure 2.6b is the schematic diagram of forming process and relative energy of these many-body states. An electron in the top of valence band jumps to the conduction band and leaves a hole in the valence band by absorbing a photon. The hole can bound with an electron in the conduction band by forming an exciton (X) or bound with two electrons by forming a negative trion (X^-). The binding energy of exciton can be written as:

$$E_{bX} = E_e + E_h + E_g - E_X \quad (2.16)$$

where $E_e = \pi^2\hbar^2/2m_e^*$, and $E_h = \pi^2\hbar^2/2m_l^* d^2$ are the energy of the free electron and the free hole, and E_X is the energy of the exciton. The binding energy of biexciton is presented as:

$$E_{bXX} = 2E_X - E_{XX} \quad (2.17)$$

The binding energy of these many-body states in TMDCs is much higher than in normal materials. According to the reported experiments results, the binding energy of biexciton is more than an order of magnitude greater than that found in conventional quantum-well structures (52 meV in WSe_2 and 70 meV in MoS_2) [24]. It is important to note that according to the theoretical calculation the high binding energy arises not only from strong carrier confinement, but also from reduced and non-local dielectric screening, in 2015, Yumeng studied the photoluminescence (PL) spectra under ultrafast pump radiation in WS_2, the experiments results are shown in figure 2.6a. The peaks are labeled by different many-body states, obviously, there are more bound states than we expect, and the emission fluency of negative trions is higher than the neutral excitons. All these results indicate that the many-body states are the dominate existence form of carriers in TMDCs.

CHAPTER 3. Experimental techniques

3.1 The Kerr effect and the Kerr signal

John Kerr discovered the Kerr effect, in as early as 1875, which describes that the magnetic materials can induce the change of the polarization and reflected intensity of incident linear polarized light. Today, most time-resolved optical experiments employ this principle to probe spin dynamics of carriers and electrons as it's the case of the experiments presented in this thesis. Two kinds of Kerr effects are normally considered, which are the electro-optic Kerr effect and the magneto-optical Kerr effect. A schematic illustration of the resultant polarization of the reflected beam under three different conditions is shown in Figure 3.1. A linearly polarized light is used as the incident beam and can be regarded as a superposition of a right-handed circularly polarized light and a left-handed circularly polarized light of the same amplitude and in phase. Upon the reflection, different sample materials, according to the band structure, have different reflectivity and propagation velocity for left- and right-handed circularly polarized light, respectively. As a result, the left- and right-handed circularly polarized components could acquire different amplitude and phase, and the resultant polarization of the reflected light can be catalogued into three cases as shown in figures 3.1. In figure 3.1a, the propagation direction of the linear beam is assumed

along z axis and its polarization direction is along y axis, the electric field vector of the left-handed light and the right-handed light can be written as：

$$\begin{cases} E_{x,\sigma^-} = E_{\sigma^-} cos(kz - wt) \\ E_{y,\sigma^-} = E_{\sigma^-} sin(kz - wt) \end{cases} \quad (3.1)$$

$$\begin{cases} E_{x,\,\sigma^+} = E_{\sigma^+} \cos(kz - wt + \pi) \\ E_{y,\,\sigma^+} = E_{\sigma^+} \sin(kz - wt) \end{cases} \quad (3.2)$$

$$\text{and } E_{\sigma^-} = E_{\sigma^+}$$

In this case, the reflectivity and propagation velocity for both components are the same, then the sum is:

$$\begin{cases} E_x = E_{\sigma^-} cos(kz - wt) + E_{\sigma^+} \cos(kz - wt + \pi) = 0 \\ E_y = E_{\sigma^-} sin(kz - wt) + E_{\sigma^+} \sin(kz - wt) = 2E_{\sigma^\pm} \sin(kz - wt) \end{cases} \quad (3.3)$$

The resultant light is still linearly polarized with its polarization direction the same as that of the incident light. The only change is in the intensity of the reflected light.

Figure 3.1b represents that the material has different reflectivity but the same propagation velocity for left- and right-handed components, so the reflected light is:

$$\begin{cases} E_x = \left(E_{\sigma^-} - E_{\sigma^+}\right)\cos(kz - wt) \\ E_y = \left(E_{\sigma^-} + E_{\sigma^+}\right)\sin(kz - wt) \end{cases} \quad (3.4)$$

$$\text{and } E_{\sigma^-} \neq E_{\sigma^+}$$

And we get:

$$\frac{{E_x}^2}{\left(E_{\sigma^-} - E_{\sigma^+}\right)^2} + \frac{{E_y}^2}{\left(E_{\sigma^-} + E_{\sigma^+}\right)^2} = 1 \quad (3.5)$$

Which is a standard equation of the ellipse with the main axis along the polarization direction of the incident light.

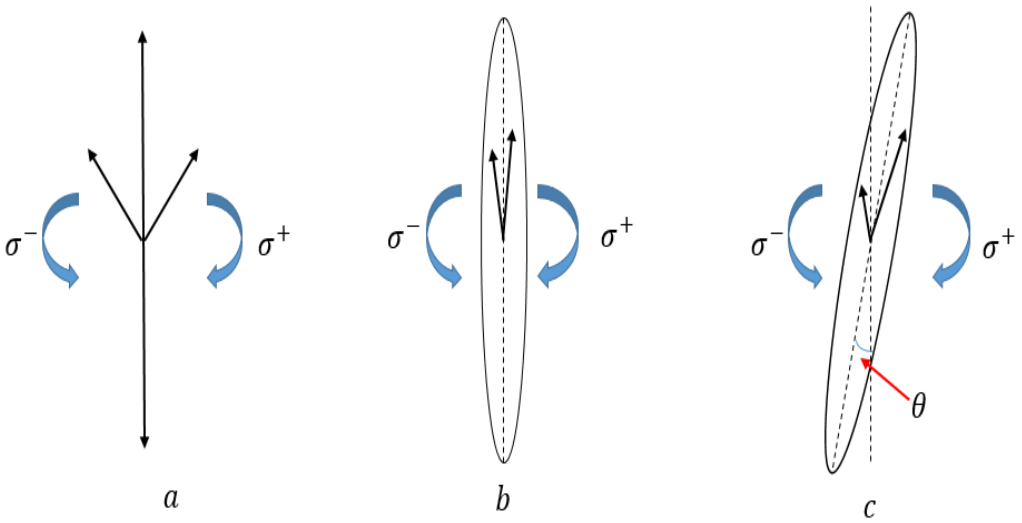

Figure 3.1 The schematic diagram of Kerr signal. (a) The left- and right-handed circularly polarized light have the same intensity and phase. (b) The left and right-handed circularly polarized light have different intensity but same phase. (c) The left-

and right-handed circularly polarized light have different intensity and different phase, and θ is called the Kerr angle.

The most ordinary case is that both the reflectivity and propagation velocity are different for the two components as in figure 3.1c, so we get:

$$\begin{cases} E_{x,\sigma^-} = E_{\sigma^-} cos(kz - wt + \varepsilon_1) \\ E_{y,\sigma^-} = E_{\sigma^-} sin(kz - wt + \varepsilon_1) \end{cases} \quad (3.6)$$

$$\begin{cases} E_{x,\,\sigma^+} = E_{\sigma^+} cos(kz - wt + \pi + \varepsilon_2) \\ E_{y,\,\sigma^+} = E_{\sigma^+} sin(kz - wt + \varepsilon_2) \end{cases} \quad (3.7)$$

$$and\ E_{\sigma^-} \neq E_{\sigma^+}$$

where ε_1 and ε_2 are the phase change. The resultant polarisation is again elliptical but with the main polarisation axis rotated by an angle, θ , with respect to the original linear polarisation direction. To obtain the standard equation for this ellipse, we project the electric field vector to the direction perpendicular to θ, $\theta_\perp$, and the direction parallel to θ, $\theta_\parallel$:

$$\begin{cases} E_{\theta_\perp,\sigma^-} = E_{\sigma^-} cos(kz - wt + \varepsilon_1)\, cos(\theta) - E_{\sigma^-} sin(kz - wt + \varepsilon_1)\, sin(\theta) \\ E_{\theta_\parallel,\sigma^-} = E_{\sigma^-} cos(kz - wt + \varepsilon_1)\, sin(\theta) + E_{\sigma^-} sin(kz - wt + \varepsilon_1) cos(\theta) \end{cases} \quad (3.9)$$

$$\begin{cases} E_{\theta_\perp,\sigma^+} = -E_{\sigma^+} cos(kz - wt + \varepsilon_2)\, cos(\theta) - E_{\sigma^+} sin(kz - wt + \varepsilon_2) sin(\theta) \\ E_{\theta_\parallel,\sigma^+} = -E_{\sigma^+} cos(kz - wt + \varepsilon_2)\, sin(\theta) + E_{\sigma^+} sin(kz - wt + \varepsilon_2) cos(\theta) \end{cases} \quad (3.10)$$

To simplify these equations, we use the equation $sin(\alpha + \beta) = sin\alpha cos\beta + cos\alpha sin\beta$ *and* $cos(\alpha + \beta) = cos\alpha cos\beta - sin\alpha sin\beta$*:*

$$\begin{cases} E_{\theta_\perp} = E_{\sigma^-} cos(kz - wt + \varepsilon_1 + \theta) - E_{\sigma^+} cos(kz - wt + \varepsilon_2 - \theta) \\ E_{\theta_\parallel} = E_{\sigma^-} sin(kz - wt + \varepsilon_1 + \theta) + E_{\sigma^+} sin(kz - wt + \varepsilon_2 - \theta) \end{cases} \quad (3.11)$$

We can make that:

$$kz - wt + \varepsilon_1 + \theta = kz - wt + \varepsilon_2 - \theta \quad (3.12)$$

So:

$$\theta = \frac{\varepsilon_2 - \varepsilon_1}{2} \quad (3.13)$$

and here we have:

$$\frac{E_{\theta_\perp}^2}{\left(E_{\sigma^-} - E_{\sigma^+}\right)^2} + \frac{E_{\theta_\parallel}^2}{\left(E_{\sigma^-} + E_{\sigma^+}\right)^2} = 1 \quad (3.14)$$

Hence, in conclusion, the different reflectivity of left- and right-handed light results in the ellipticity of the reflected light, while the phase change contributes to the Kerr rotation.

3.2 Time-Resolved pump-probe measurements

Figure 3.2 is the schematic diagram of the time-resolved pump-probe experiment setup. The light source is a Spectra-Physics Mai-Tai Ti: Sapphire oscillator with 250 fs pulse duration, 80 MHz repetition rate, 1W average power, and wavelength tunable between 760 nm to 880 nm. An optical-electro cell (2) is placed just at the beam exit to stop any reflection back to the laser cavity which would disturb the laser operation and cause power fluctuation. Each laser pulse is split into two pulses by a beam-splitter

(3). The green line indicates the path of the transmitted pump pulse. The path length of the pump pulse is delayed by an optical delay line (5) and it is modulated by the optical chopper (4). The polarization of the pump pulse is varied between linear and circular by adjusting the angle between the optical axis of the polarizer (p1) and quarter-wave plate (w1). The intensity of the pump pulse is adjusted by the density filter wheels (a2). Finally, the pump pulse is focused onto the sample surface with an achromatic doublet with focal length 75 mm, and the spot size of the pump is about 30 μm.

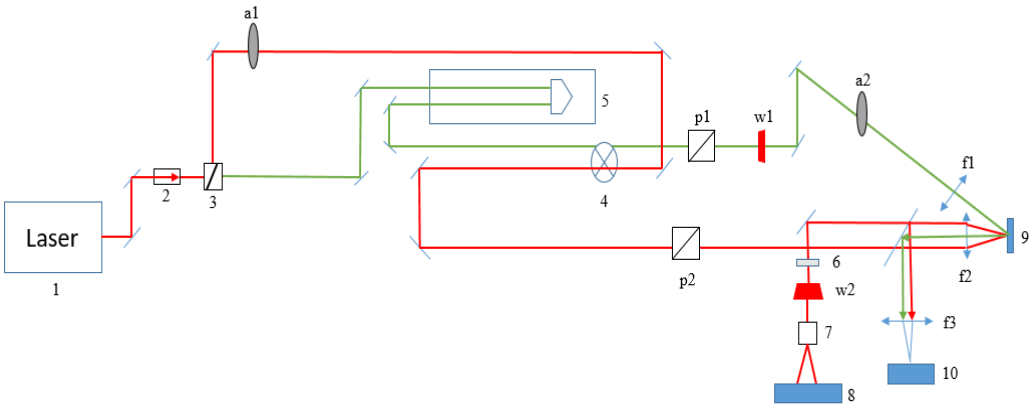

Figure 3.2 The schematic diagram of the time-resolved pump-probe experiment setup. 1: MAITAI laser; 2: isolator; 3: beam splitter; 4: dual frequency chopper; 5: delay line; 6: filter; 7: Wollaston prism; 8: photodiode detector; 9: sample; a1, a2: attenuator; 10: CCD camera; f1, f2, f3: focus lens; w1: quarter waveplate; w2: half waveplate.

The intensity of the probe pulse is adjusted by the density filter wheels (a1), and it is also modulated by the optical chopper (4). The focal length of focus lens (f2) is 13 mm, which ensures the spot size of probe is much smaller than the pump. The pump

pulse is to excite electrons from the valence to the conduction band of the semiconductor. The state of excitation depends on the sample material's band structure and the property of photon. The probe pulse arrives at the same position of the sample surface after a delayed time. As the optical select rule is the same as the first pulse, any changes of carriers or electrons' spin caused by the first pulse are probed by the second pulse. The time delay between the excitation and probing is controlled by the delay line's movement with a resolution of order of 1 femtosecond. However, since the laser's pulse width has the magnitude of 100 femtoseconds, generally, the resolution time is of the same magnitude.

3.3 Pump-probe delay line

Figure 3.2a presents the optical delay line with a travel range of 300 mm used in our experiments. The speed of light in vacuum is approximately 3×10^8 meters per second which means the maximum time delay range is:

$$\frac{300\times10^{-3}\ m}{3\times10^8\ m/s}\times2 = 2000\ picosecond$$

And the time resolution for our delay line is:

$$\frac{0.1\times10^{-6}\ m}{3\times10^8\ m/s}\times2 \approx 0.667\ femtosecond$$

It is the essential that the incident beam is set parallel to the orientation of the translation motion of the delay line. This is to ensure that the movement of retroreflector prism will not result in the shift of the emergent light. The retroreflector prism reflects a beam back toward its original direction via three total internal reflections, and the beam will be inverted and reflected through 180° even if the angle of incidence is not zero. However, as show in figure 3.3b, if the angle of incidence is not zero, the emergent light will have a displacement when the prism moves.

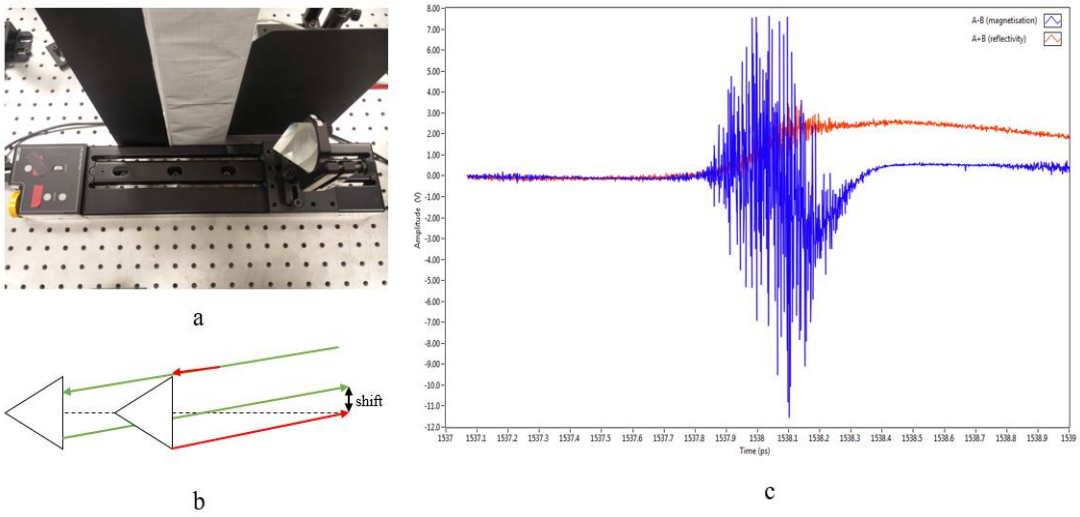

Figure 3.3 (a) The picture of the long-travel stage and retroreflector prism used in the experiment. The travel range is 300 *mm, and the minimum achievable incremental movement is* 0.1 *μm. (b) The schematic diagram of the displacement of the emergent light as the retroreflector prism moves. (c) The time-domain scan data around the zero delay point between the pump and probe. The step size is 1 femtosecond, the blue line is the Kerr signal and the red line is reflectivity.*

Figure 3.3c is the time-domain scan data obtained from an intrinsic GaAs sample. The obvious fringes both in the reflectivity and Kerr signal are caused by the interference

between the reflected probe and the scattered pump light. These interference fringes can be observed within the duration of the cross-correlation function of pump and probe pulses. The duration of the fringes is approximately 500 femtoseconds which indicates a 250 femtoseconds pulse width. Moreover, these oscillations have a period of about 1 femtosecond, which is the same as the experimental step size we set. Therefore, we can consider it as the experimental "artefacts", and it allows an easy determination of the zero delay position even if the sample has no signal.

3.4 Chopper and Lock-in amplifier

The standard ultrafast pump-probe experiment often requires detecting very small signals, of the order of 1 μV (Kerr signal) or 1 mV (reflectivity), while the background signal usually has the order of 1 V. Generally, the small signals are accompanied by background noise of the order of 10 mV [25]. To detect such a small signal on top of a large noisy background, modulation of the pump beam at a fixed frequency, Ω, is typically employed. The signal induced by the pump beam therefore has the same frequency of Ω, and this frequency is used as the lock-in amplifier's reference frequency. The basic principles of a lock-in amplifier relies on the orthogonality of sinusoidal functions. It means when a sinusoidal function of frequency Ω_1 multiply another sinusoidal function of frequency Ω_2 and integrated over a time much longer than the period of the two functions. If $\Omega_1 \neq \Omega_2$, the result will be zero; if $\Omega_1 = \Omega_2$ and the two functions have a constant phase relation, the average value is equal to half

of the product of the amplitudes of the two sinusoidal functions. Therefore, for any periodic random noise, as it can be decomposed into the sum of a set of sinusoidal functions, the result is still zero. Theoretically, the lock-in amplifier synchronized with the reference frequency Ω would only extract the signal induced by the pump beam.

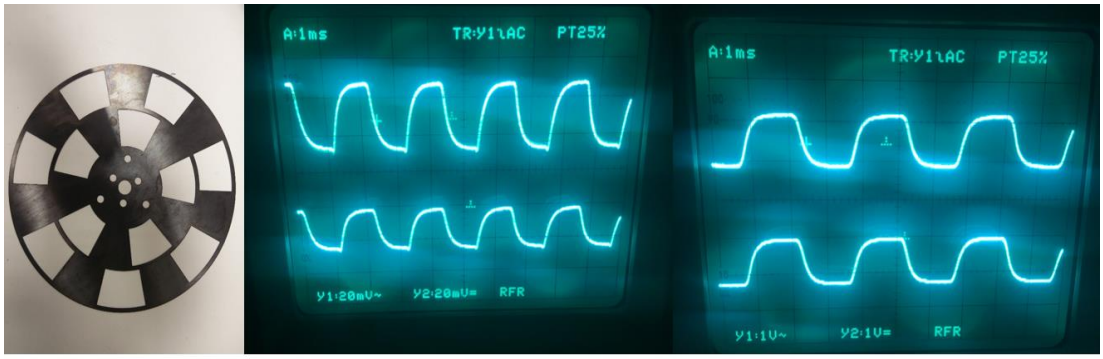

a b c

Figure 3.4 (a). Dual frequency optical chopper blade we used in experiments, the inner slots are 5 and the outer slots are 7. A chopper head drives it with a frequency Ω, so the inner frequency is 5Ω *and the outer frequency is* 7Ω*.(b) The scattered pump beam signal is monitored by the oscilloscope with probe beam blocked. The frequency is* $469\ Hz$*, and the first channel is the signal of detector A, with the amplitude of* $40\ mV$*, the second channel is the signal of detector B, with the amplitude of* $20\ mV$*. (c) The probe beam signal with a frequency of* $335\ Hz$*, and the amplitude for both channels is* $1.4\ V$*.*

However, a single modulation of the pump beam won't work unless a dual-frequency optical chopper blade is used as shown in the figure 3.4a. The main problem is that not only the probe beam but also the scattered pump beam enters to the detector. We use an oscilloscope to monitor photodiodes' output signals with the dual-frequency

chopper is set in the set-up and rotates at a frequency of Ω. The chopper blade has two sets of slots with the inner slot set modulating the probe beam at a frequency of 5Ω and the outer slot set modulating the pump beam with a frequency of 7Ω. The figure 3.4b is the screen shot of the output signal of the detector with pump light on only, and figure 3.4c is the signal with the probe light on only. Although the probe signal is about $1\ \mathrm{V}$, the scattered pump light produces a signal with a magnitude as big as $20\ \mathrm{mV}$. This 20 mV has the same frequency as that of the signal induced by the pump beam in a signal modulation of pump beam, while the latter is 20 times smaller in magnitude. Therefore, the scattered pump beam gives rise to a huge background signal. Furthermore, the pump beam goes through the optical delay line which would cause unavoidable small change in propagation direction even though the pump beam is optimizing aligned with respect to the retroreflector prism. The scattered pump beam would be shifted when the delay line moves. which causes the background signal from the scattered pump beam is a function of the delay time. As a consequence, single modulation cannot eliminate the scattered pump beam's noise.

In order to eliminate the noise from the scatter pump beam, both the pump beam and the probe beam should be modulated, so that the Lock-in amplifier's reference frequency can be chosen to be different from the modulation frequency of the pump beam. The probe beam is modulated by the inner slot set with a frequency of $5\Omega = 335\mathrm{Hz}$, and the pump beam is modulated by the outer slot set with a frequency of $7\Omega = 469\mathrm{Hz}$. The chopper controller provides three different frequency outputs, the DIFF frequency ($7\Omega - 5\Omega = 2\Omega$), the SUM frequency ($7\Omega + 5\Omega = 12\Omega$), and the

OUTER frequency (7Ω). We have done a series of experiments with different reference frequency in a GaAs test sample, the reflectivity data is shown in the figure 3.5.

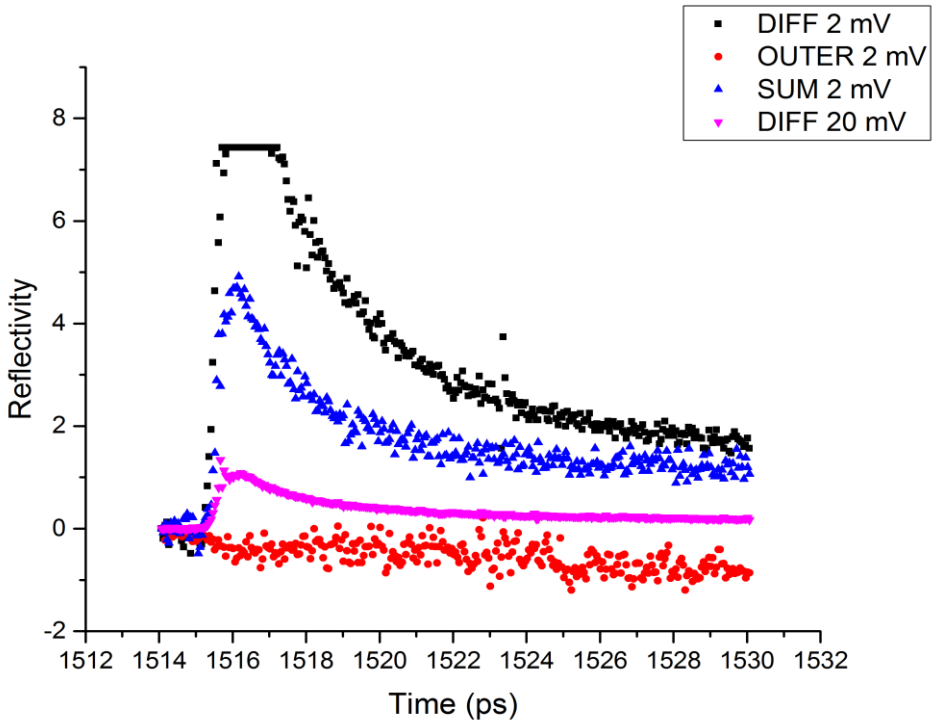

Figure 3.5 The raw data of chopper test in a GaAs sample. The DIFF and SUM both reveal the signal, but have different numerical magnitude. However, the OUTER has no signal but a slight drift with the time. When use the DIFF as the reference frequency and the sensitivity is only 2mV, the output signal exceeds the Lock-in dynamic range as set.

Compare the reflectivity signal obtained with Lock-in reference frequency using between the OUTER frequency (7Ω) and the DIFF frequency (2Ω) both at a sensitivity of 20 mV, the OUTER just show a lot more noise with a slightly drift while the DIFF reveals a time-resolved reflectivity change. While using the DIFF (2Ω)and the SUM

(12Ω) frequency with a lock-in sensitivity of 2 mV, both cases reveal the signal but with different signal strength. The DIFF signal is approximately 3 times larger than the SUM signal. To understand why there is a significant difference between this two signal, the following simulation result gives a clear explanation. The source code and comments are in the appendix.

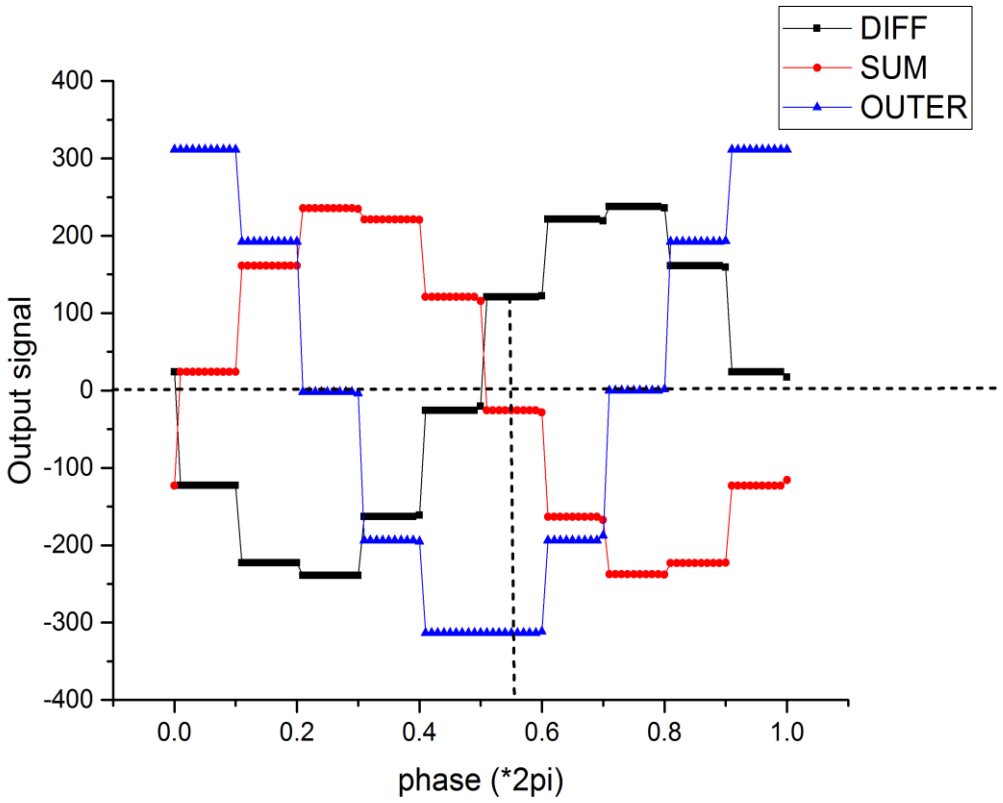

Figure 3.6 The simulation result for different reference frequencies. The x-axis is the phase change between pump and probe, from 0 to 2π; the y-axis is the lock-in amplifier's output signal. The vertical dash line is the phase change between pump and probe in our experiments, and the horizontal dash line is y equal to zero.

Two sinusoidal functions are used to simulate the pump and probe beam after chopper:

$$\text{probe: } A(t) = \sin(2\pi \times 5\Omega t) \quad (3.15)$$

$$\text{pump: } B(t) = \sin(2\pi \times 7\Omega t + 2\pi j) \quad (3.16)$$

here $2\pi j$ is the phase change between probe and pump. Only when the pump beam and the probe beam arrive on the sample, can we get the signal induced by the pump. Therefore, we set when $A(t) > 0$ and $B(t) > 0$, the signal $C(t) = 1$, else the signal $C(t) = 0$. Here we get a square wave form signal, which is the same as the signal in the experiment. Then we modulate this signal with different reference frequencies, and the output signal is the time integration.

$$U(t) = \int C(t) \times \sin\left[2\pi \times (FRQ)\right] dt \quad (3.17)$$

As shown in the figure 3.6, the DIFF signal and the SUM signal change with the phase between the modulated pump and probe beams, and if we rotate the DIFF or the SUM $180°$ along the $x = \pi$ line, they will coincide. In our experiments, the phase difference between pump and probe beam is approximately 0.55π as shown in the vertical dash line, which is set by the arrangement of the two sets of slots on the chopper blade. The simulation DIFF output signal at this phase point is 120.909, while the SUM output signal in this point is -25.864. Since the lock-in amplifier we used in the experiments has the auto-phase setting, the output signal will be positive, so the DIFF signal is approximately 3.6 times larger than the SUM signal.

3.5 The Image and detect system

3.5.1 The Image system

An image system is constructed to make sure the pump and probe spatially overlapped on the sample surface. The pump and probe beams are focused to about 30 μm and 8 μm in diameter, respectively, and the $MoSe_2$ samples are grown as triangle islands on Si substrates with island dimensions ranged from $10 - 100$ μm. The image system is essentially the same as an optical microscope, and the magnification factor equals to the ratio between the focal length of eyepiece lens to that of the objective lens.

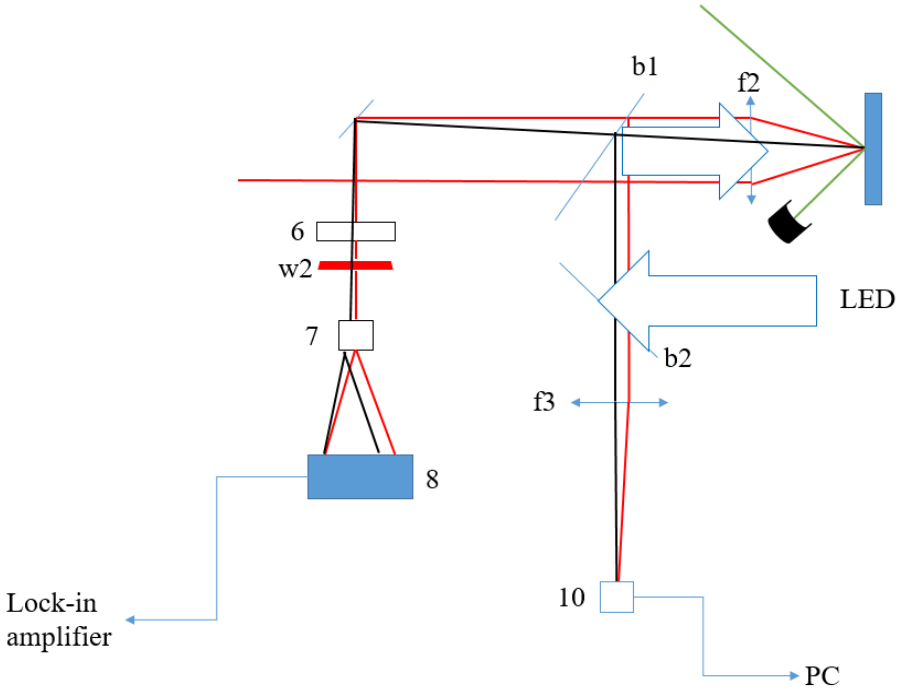

Figure 3.7 The schematic diagram of the image and detection system. 6: filter; 7: Wollaston prism; 8: photodiode detect; 10: CCD camera; b1, b2: pellicle beam splitter; f2: objective lens; f3: eyepiece; w2: half waveplate.

Figure 3.7 is the schematic diagram of the image and detection system. The green line is the pump beam path, the red line is the probe beam path, and the black line is the scattered pump beam path. The focal lens f2 focus the probe beam onto the sample and collimate the reflected probe beam from the sample. Part of the probe beam is reflected by the beam sampler (b1) and focused onto the CCD (10) by the eyepiece lens f3. The rest of the probe beam is transmitted and directed to the detection system. The pump beam is oblique incidence and only the scattered pump light form the sample get collected by the f2 and then focused onto the CCD. Thus the pump spot looks much dimmer than the probe spot on the CCD image. If the sample's optical scattering is not strong enough, we even cannot see the pump spot. White light from a LED source with a wavelength of 450 nm is directed to illuminate the sample by a second beam sampler and the f2. Both beam samplers are two pellicle beam splitters with thickness of $2\,\mu m$, so when we remove them during measurements without introducing a noticeable optical path length difference and displacement of the probe beam. The transmission/reflectivity rates of b1 and b2 are 92:8, and 55:45, respectively. Unfortunately, since the pump and probe beams' wavelength (around 800 nm) is different from that of the LED light, so the focus point of the LED light is different from the pump and probe beams' focus point, and the difference is 0.89 mm. In other words, when we can see the pump and probe in the image, we cannot see the sample clearly; when we can see the sample clearly, the pump and probe beams are not focused. That is not a problem in a continuous film or bulk sample, but for the $MoSe_2$ samples of very small monolayer triangles with side length no more than

100 μm, a tightly focused image is essential as shown in figure 3.8. We tried to replace the blue light to a white light, however, it does not solve the problem. Therefore, the wavelength of the LED maybe not the only reason.

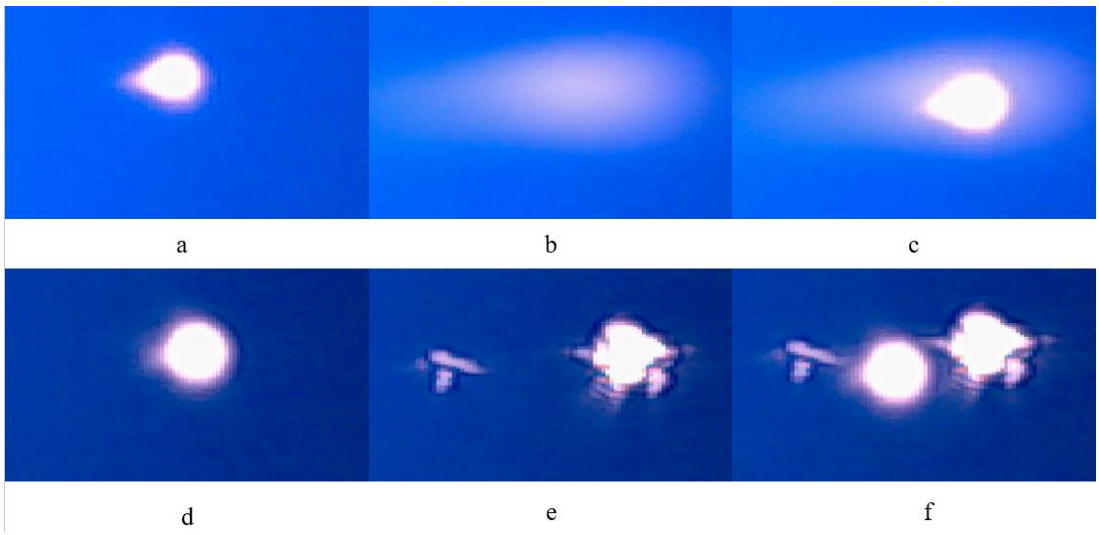

g

Figure 3.8 (a) The probe spot on the GaAs sample. (b) The pump spot on the GaAs sample. (c) The pump and probe overlapping on the GaAs sample. (d) The probe on the $MoSe_2$ sample. (e) The pump spot on the $MoSe_2$ sample. The pump light is mainly

scattered by the black impurity which is unevenly distributed. (f) The pump and probe overlapping in the $MoSe_2$ sample. (g) The image of the $MoSe_2$ sample under LED light. The triangles in this image are the monolayer $MoSe_2$, the contrast ratio between the sample and the substrate is very low due to the low reflectivity of the monolayer sample. The red ellipse area indicates where the pump and probe spots are. The red arrow points out the black impurity, which scatters the pump beam and formed its images in the figure (e) and (f).

Fortunately, impurities in the $MoSe_2$ sample help us in positioning. Figure 3.8a shows the probe spot on the intrinsic GaAs sample, and figure 3.8b shows the pump spot on the intrinsic GaAs sample, as the intrinsic GaAs has the fluorescence effect, the image still shows the pump's position even though its reflected beam does not reach to the CCD camera. However, neither the $MoSe_2$ sample nor its Si substrate has the fluorescence effect. Therefore, we cannot see the pump spot on the $MoSe_2$ sample unless it was scattered by the impurities. First of all, we put the $MoSe_2$ sample next to the GaAs sample, and adjust the pump's position to make the pump and probe both in focused and overlapped on the GaAs sample, just like in figure 3.8c. It is the important step which make sure the overlapping of the two spots only happen when either of them is in focus. Then the sample holder is adjusted horizontally until the pump and probe arrive the area pointed out in figure 3.8g. Because the pump is scattered by the impurities so the scattered pump beam helps us to locate where the sample triangle is. Then the sample holder is adjusted to make sure the probe spot is in focus so as to make sure the overlapping between the pump and probe, as shown in figure 3.8e.

3.5.2 The detection system

The detection system is an optical bridge measurement system which consists a filter, a half waveplate, a Wollaston prism, and 2 photodiode detectors. The filter is laser line filter with a bandpass range FWHM of 10 nm and the transmission less than 0.01% in its cut-off range, which blocks stray light at wavelength different from its central line significantly. The half waveplate rotates the polarization of the incident light, as shown in figure 3.8a, so as to balance the projection of the incident light field along the x-axis and y-axis after the Wollaston prism, as shown in the figure 3.8b.

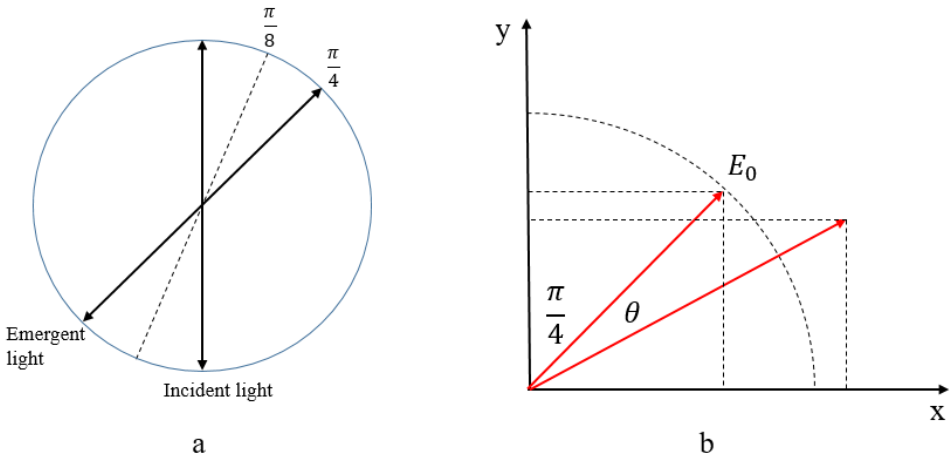

Figure 3.9 (a) The effect of the half waveplate is to mirror the incident light's polarization vector through its fast axis. (b) The Wollaston prism splits the incident light's x-component and y-component into two outputs, and they are in the same plane.

As shown in figure 3.9b, the light field of the reflected probe beam without the pump beam on is E_0. Its polarization axis is set along $\pi/4$ orientation with respect to the optical axis of the Wollaston prism by rotating the half wave-plate, to balance its x

and y components. After passing through the Wollaston prism, the intensity of the probe beam, I_0, is split into two beams with equal intensity and detected by two photodiodes. The output signals of the two detectors, A and B, have the same magnitude just as shown previously in figure 3.4c. When a pump pulse arrives at the sample just before the probe pulse, the reflected probe pulse may have a change in the intensity and polarization direction. In figure 3.9b, we assume that the intensity changes by ΔI and the polarization direction rotates by θ, therefore, the change in the output signals A and B are:

$$\mathrm{A} = \left(I_0 + \Delta\mathrm{I}\right)\cos^2\left(\frac{\pi}{4} - \theta\right) - I_0\cos^2\left(\frac{\pi}{4}\right) \quad (3.18)$$

$$\mathrm{B} = \left(I_0 + \Delta\mathrm{I}\right)\sin^2\left(\frac{\pi}{4} - \theta\right) - I_0\sin^2\left(\frac{\pi}{4}\right) \quad (3.19)$$

in our experiments, the direction change $\theta \ll 0.1$ rad, so we use the approximation: $\cos\theta \approx 1, \sin\theta \approx \theta$, then we get:

$$\mathrm{A} + \mathrm{B} = \Delta\mathrm{I} \quad (3.20)$$

$$\mathrm{A} - \mathrm{B} = 2I_0\theta + 2\Delta I\theta \quad (3.21)$$

In each experiment, $I_0 = \text{constant}$, and $2\Delta I\theta$ is the high order minim, so the $\mathrm{A} + \mathrm{B}$ signal is the change of the reflectivity and the $\mathrm{A} - \mathrm{B}$ signal is the Kerr rotation.

Chapter 4. Results and conclusion

4.1 GaAs results

A 80 MHz optical parametric oscillator with a pulse width of 250 fs and the average power of about 0.7 W is used for time-resolved measurements. The laser wavelength is tunable from 770 nm to 860 nm. A piece of an intrinsic GaAs wafer is used as a test sample after the completion of the entire time-resolved experiment setup. As GaAs has been studied for several decades, and it has a direct band gap, whose energy is within our laser's tuning range, it is an ideal material for testing the system. First of all, the time-resolved reflectivity/Kerr rotation measurements at a fixed 800 nm wavelength have been carried out as a function of pump fluency.

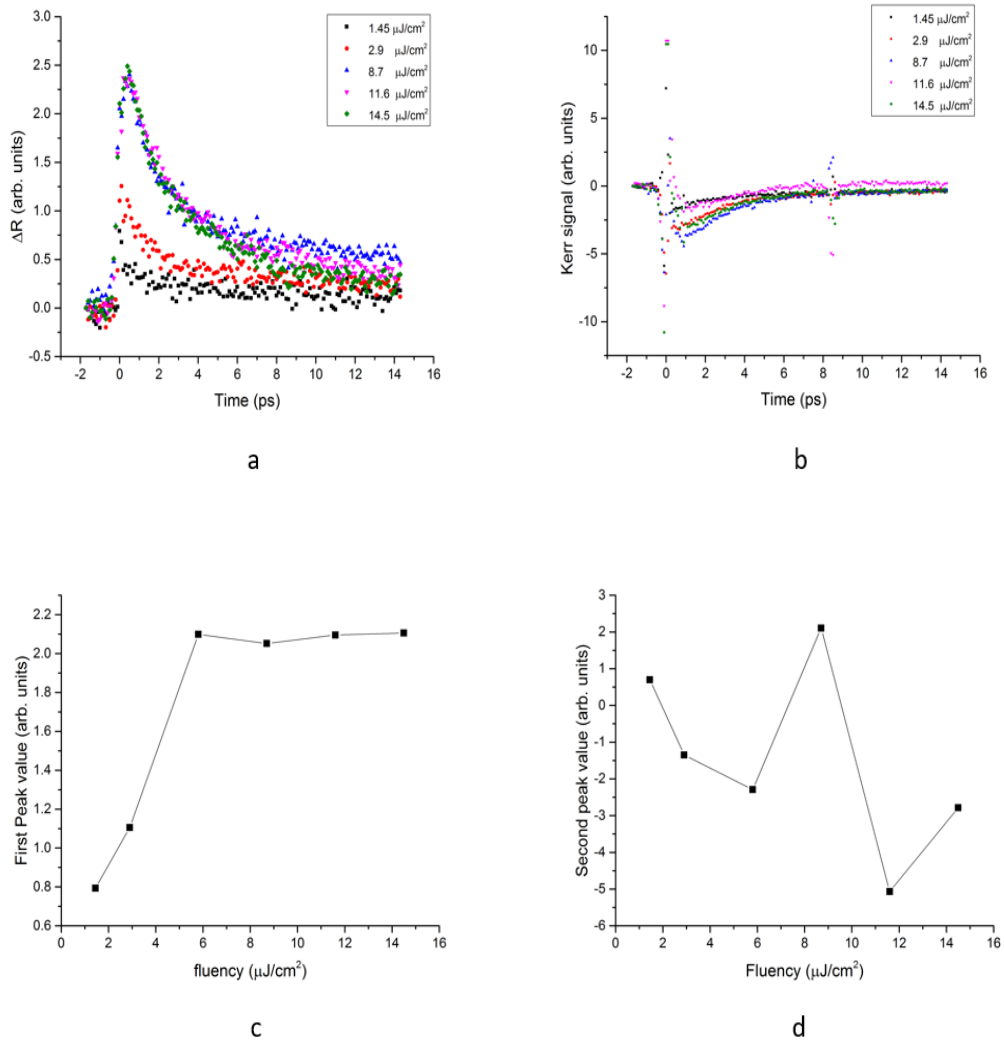

Figure 4.1 The time-resolved measurements as a function of pump fluency in an intrinsic GaAs sample. (a) The transient reflectivity spectra. (b) The transient left-handed pump Kerr signal. (c) The first peak's value vs pump fluencies. (d) The second peak's (about 8 ps) value vs pump fluencies.

For all measurements, the pump has 3 different helicities, left-, right-handed circular polarized, and linear polarized, while the probe is linear polarized. The pump beam is focused to about 30 μm, therefore 1 mW pump power corresponds to a pump fluency for each pulse about 0.29 $\mu J/cm^2$. According to previous experiments results, the

pump fluency on the GaAs samples is between 1 and 10 μJ/cm^2, producing a spatially averaged electron-hole pair density of 10^{17} to 10^{18} cm^{-3} at the band-gap resonance [26]. The pump fluency is varied between 1.45 and 14.5 μJ/cm^2, and the results are shown in the figure 4.1. The pump excited electrons occupy the transition state and reduce the probe photon absorption, which is called the Pauli blocking [12]. The excited electrons also recombine with the hole in valence band by sending a photon and these two effects produce the first peak of the transient reflectivity spectrum. These two effects are related to the fluency and the density of participating state. When the pump power is about 1μJ/cm^2, the pump induced electrons has an electron-hole pair density about 10^{17} cm^{-3}, which are not enough to occupy all the transition states, and the pump induced radiation is low, therefore the transient increase in the probe reflectivity is low. For the pump power is equal or greater than 8.7 μJ/cm^2, all the transition states are occupied, and the pump induced radiation reaches its maximum. Therefore, the transient peak of the probe reflectivity at these pump power has the same magnitude as shown in the figure 4.1 (c).

Figure 4.1b shows a transient left-handed pump Kerr signal. A significant observation is that there are a second peak in all curves obtained at different pump fluency. All these second peaks occur at the same time delay of 8 ps after the pump excitation, and the height of these peaks are not related to the pump fluency. In fact, the second peak also exists in the reflection spectra, but more obvious in the Kerr signal. We don't know what attributes to these second peaks, however, adding a narrow bandwidth filter

before the detector can eliminate these peaks. So a narrow bandwidth filter is added for all the following experiments.

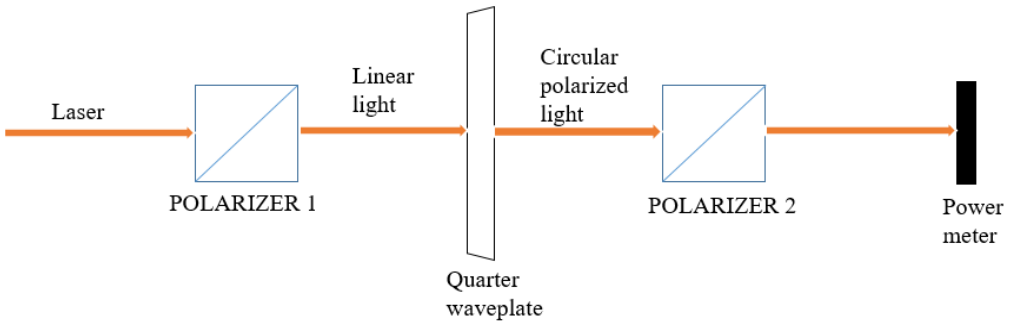

800 nm pump	Left-handed	Linear	Right-handed
Max power (mW)	4.996	8.550	5.099
Min power (mW)	3.337	0.011	3.315
Ratio	0.668	0.001	0.650

Figure 4.2 The top diagram is the inspect method of circular polarized light and the bottom table is the result.

The main problem for helicity test in our experiments is that we cannot get pure σ^+ or σ^- photons. Table 4.1 shows the method used to inspect the circular polarized light. The left- or right-handed circular polarisation is produced by the polarizer 1 and the quarter waveplate. The polarisation state is then checked by the polarizer 2 and the power meter before performing the actual measurements. Then the polarizer 2 is rotated through 360°, and the maximum power and the minimum power are noted, as shown in figure 4.2. The ratio between minimum powers and maximum powers is about 0.65 for all measurements.

Figure 4.3 shows the time-resolved reflectivity /Kerr rotation measurements and the multi-exponential fitting results performed with different pump helicity of the GaAs

sample. The pump and probe wavelength is fixed at 800 nm, the polarisation of probe is fixed at linear, and the pump fluency is fixed at $11.6\ \mu J/cm^2$. In figure 4.3a, the peak magnitude of the transient intensity obtained under three different pump polarisation are different, with the highest reflectivity peak under the linear pump excitation and the lowest reflectivity peak under the right-handed pump excitation. The magnitude of the reflectivity peak under the linear pump excitation is about half way between those under the two circular polarisation. This trend exists in all measurements with different pump helicity. The tri-exponential decay function ($\Delta R = A \cdot \exp(-t/\tau_1) + B \cdot \exp(-t/\tau_2) + C \cdot \exp(-t/\tau_3) + D$) is used for fitting the reflectivity data, which gives 3 time parameters: $\tau_1 \sim 1.5\ ps, \tau_2 \sim 10\ ps, \tau_3 \sim 100\ ps$, which are similar to what have been reported. Figure 4.3b is the Kerr signal data with different helicity pump. Obviously, the Kerr signal for right-handed pump is positive, for left-handed pump is negative, and almost none for linear pump. The Kerr signal is well fitted by the bi-exponential decay function ($\Delta R = A \cdot \exp(-t/\tau_1) + B \cdot \exp(-t/\tau_2) + C$). Two decay times τ_1 and τ_2 for different pump helicities are found to have the approximately same results of 3 ps and 30 ps, respectively.

We now try to interpret why the peak magnitude of the reflectivity data induced by different helicities pump has remarkable difference. For the linear light containing equal numbers of σ^+ and σ^- photons, it can excite both the spin up and down electrons in the top of valence band according to the optical transition selection rule. Therefore, when all the transition states are occupied, this will result in the absorption of the probe's σ^+ and σ^- photons decreased significantly. For left- and right-handed

pump, they only result in the decrease of the corresponding helicity photons' absorption, thus, the linear pump should induce the highest peak magnitude in the reflectivity data for linear probe. In our data, the peak magnitude in the reflectivity is highest for right-handed pump, then middle for linear pump, and lowest for left-handed pump. This seems indicate an unbalanced electron spin polarisation at the top of the valence band of the GaAs test sample. However, the peak magnitude in the Kerr rotation data is almost the same between the right- and left-handed pump data, which indicate a balanced electron spin polarisation distribution. To understand the reflectivity data, further measurements with different probe photon energy is need, which would be reflected in the future work at the end of this thesis.

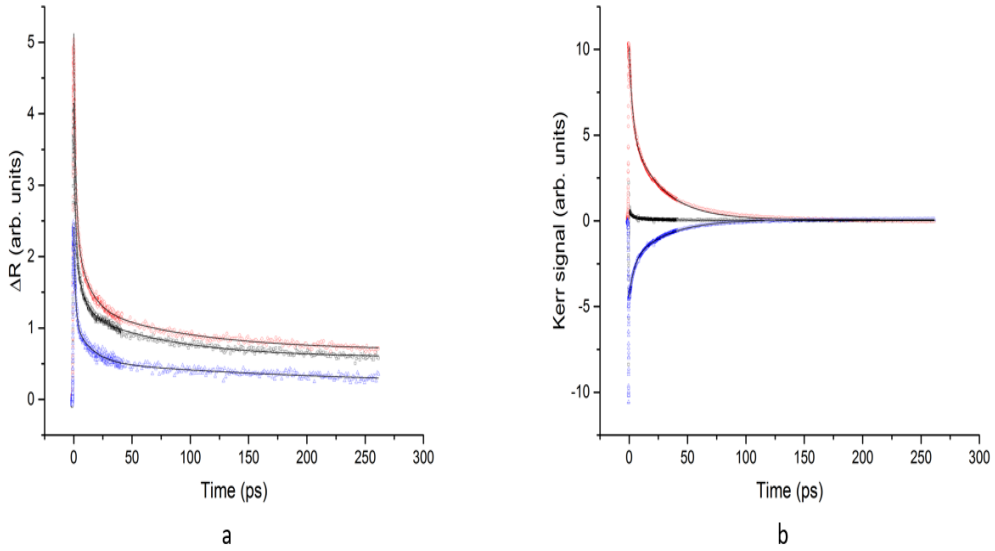

Figure 4.3 The experiments results of GaAs. The pump and probe wavelength is 800 nm, and the pump photons have 3 helicities, right-handed, left-handed and linear: black—left-handed pump, red—linear pump, blue—right-handed pump. The dots are experiments data, and the solid line is the fitting results. (a) The transient reflectivity

spectra. The data is fitted by tri-exponential decay function. (b) The transient Kerr signal spectra. The data is fitted by bi-exponential decay function.

Time-resolved reflectivity under different pump wavelength has also been carried out to test the bandgap of intrinsic GaAs as shown in figure 4.4. The transient reflectivity increase has been observed for pump wavelength at 780 nm, 790 nm, 800 nm, 810 nm and 820 nm with the highest peak magnitude occurring at 800 nm pump wavelength. For the pump-probe measurements, only the pump induced reflectivity can be detected. Hence, the pump induced reflectivity will start to increase as soon as the photon energy is higher than the band gap energy, and it will be decreased when the photon energy is too larger compared to the band gap energy. Therefore, the band gap of GaAs in room temperature is about 820 nm as the transient reflectivity starts to show an appreciable peak at 820 nm wavelength.

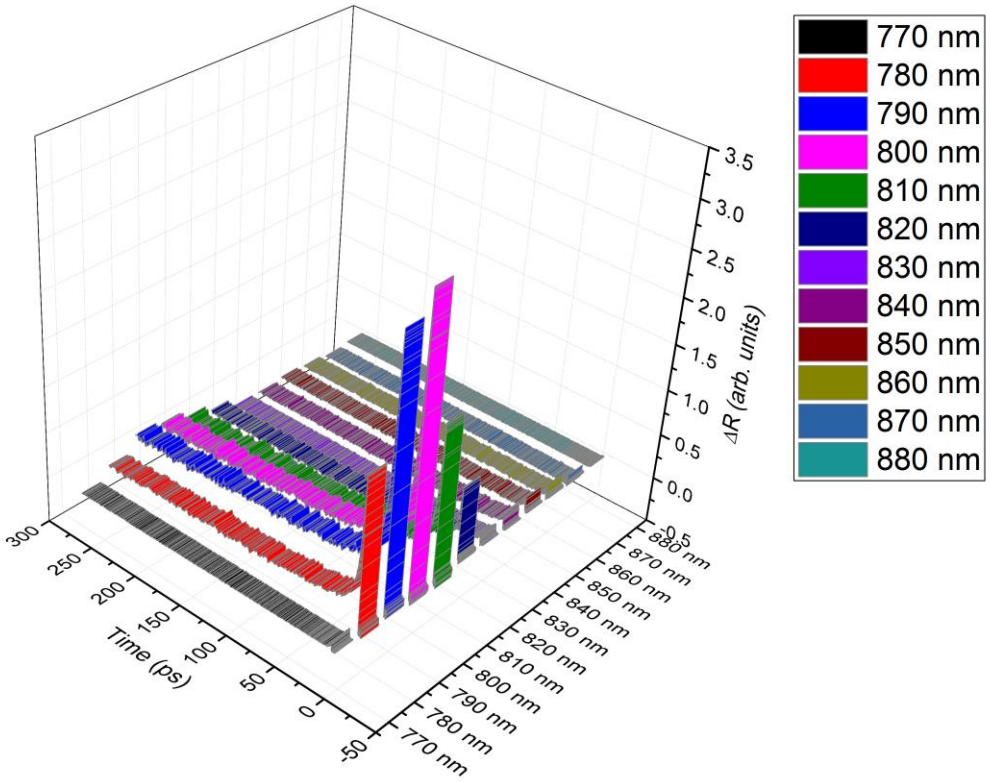

Figure 4.4 time-resolved reflectivity spectrum of the intrinsic GaAs under different laser wavelength. The pump light is linear polarized with a fluency of 40 mW.

4.2 $MoSe_2$ results

We move on to study $MoSe_2$ after the measurements on the GaAs test sample which assure the commission of the set-up. Figure 4.5 shows the transient reflectivity spectrums of monolayer $MoSe_2$ for different laser wavelengths but both pump and probe always keep the same wavelength. The dots are the experimental data, while the solid lines are the bi-exponential decay fitting results. Three kinds of helicity photons are used to pump the sample, left-handed, right-handed and linear, respectively. When comparing each figure in figure 4.5, a remarkable observation is

that the transient reflectivity spectrums have a strong dependence on laser wavelengths. For 790 nm pump and probe, the ΔR induced by pump is always positive during the whole course of measurements, while for 800 nm, 810 nm and 820 nm, the pump induced ΔR falls very quickly from the positive peak to negative, and the decay speed increases as the photon energy decreases.

This phenomenon has been reported in monolayer MoS_2. Qinsheng Wang and his team reported their two-colour experiments result in 2013. The pump energy of their experiments is higher than the band gap of MoS_2 while the probe energy is very close to the A exciton's energy. They attribute the negative part of ΔR to the band gap renormalization effect due to the coulomb interactions of the dense electron-hole plasma [27]. Another team did the same non-degenerate measures in monolayer WS_2 at room temperature, and they attribute the negative part to the bound trion [28]. However, in our experiments, the pump energy is the same as the probe energy, which is called the one-colour or degenerate measurement. As we discussed in chapter 2.4, the band gap of $MoSe_2$ is about 1.56 eV (790 nm) at 0 K, when the pump and probe energy is significantly lower than the band gap energy, the pump cannot excite the electrons in valence band, so there is no electron-hole plasma which contributes to the band gap renormalization and the bound trions. The transient reflectivity peak obtained at laser wavelength down to 820 nm in figure 4.5 is still very strong indicates that the band gap energy of $MoSe_2$ has a relatively great reduction in the room temperature compared to its value, 790 nm, at zero Kelvin. In GaAs, the reflectivity spectra show a very strong peak about 820 nm, however, the peak declines markedly

as the photon energy decreases further. Therefore, the bandgap energy of $MoSe_2$ is very likely to be lower than 1.5 eV (820 nm).

The transient reflectivity data goes from positive to negative when the wavelength is longer than 800 nm. For the high energy pump and probe, the excited electrons have a high energy, which ensures it stay in the conduction band longer than the electrons in the bottom of conduction band, even if it is scattered by phonon, other electrons or impurities. These electrons have a contribution to the reflectivity, when they come back to the valence band by sending photons. Hence, the reflectivity decline speed increases as the photon energy decrease.

As shown in figure 4.5, the temporal profile for all three different pump helicity is similar, except those of 800 nm. The unexpected phenomenon is that the peak magnitude of the reflectivity data is strongly dependent on pump helicity. For 790 nm and 800 nm, the right-handed pump peak is lowest; for 810 nm, the left-handed pump peak is the lowest; while for 820 nm, it is the linear pump peak. We consider this helicity-dependence phenomenon is due to the asymmetry of the band structure near the Dirac points. As we discussed above, the bandgap energy of $MoSe_2$ in room temperature is likely lower than the 820 nm photon's energy. Thus, for high energy photons, they can only be absorbed by the lower energy electrons in the valence band. The absorbing of σ^+ or σ^- photons is related to the band structure and the polarisation of the density of the states. For example, the states that can absorb σ^+ photons are much more than the states absorbing σ^-. photons, then the σ^+ pump will induce a

higher peak in transient reflectivity, and vice versa. Of course, this assumption requires further experiments to put it on a solid foot, which will be reflected in the future work.

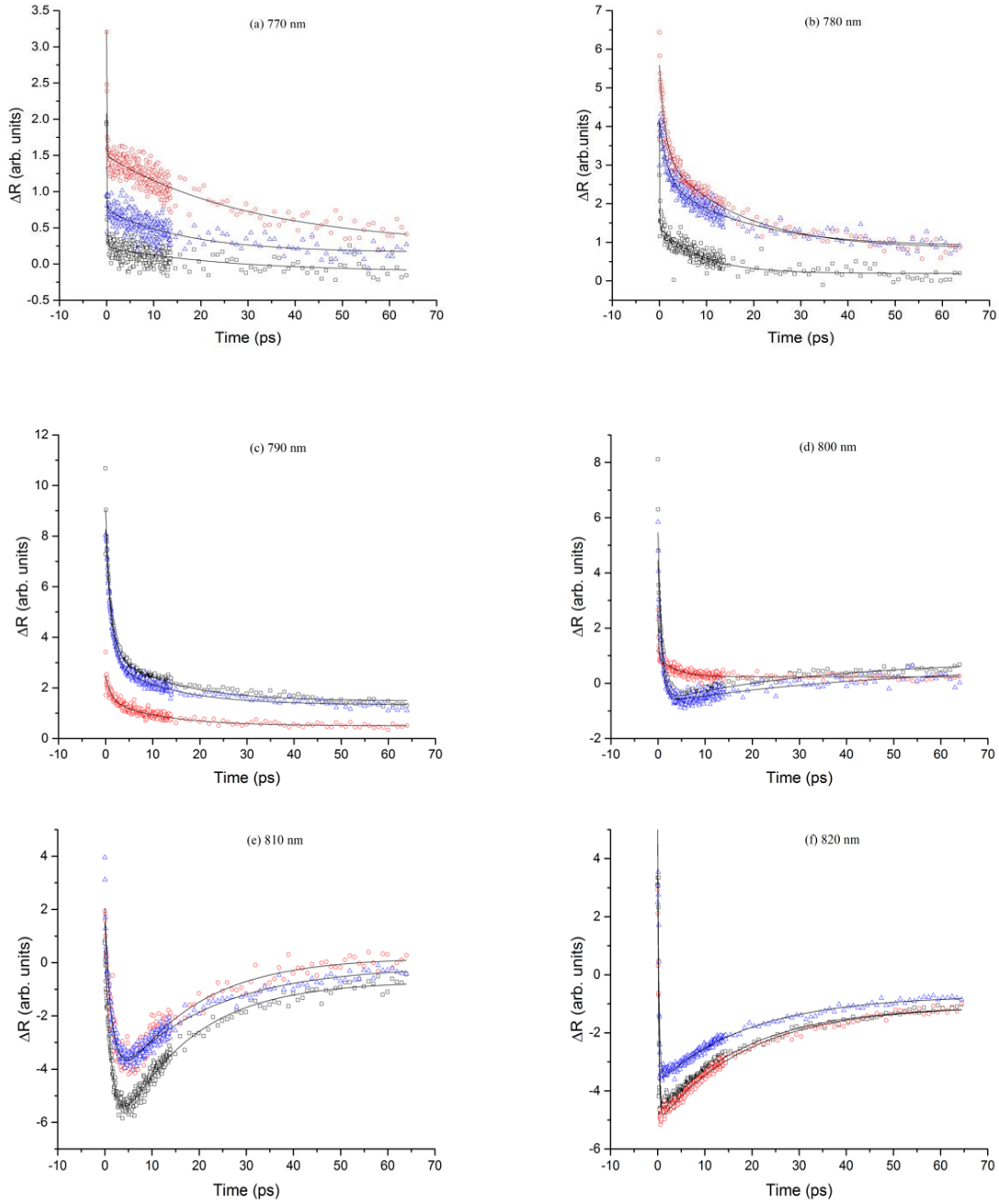

Figure 4.5 The transient reflectivity spectrum of MoSe2 for different wavelengths at room temperature. The solid lines are the bi-exponential decay fitting results. (a) 790 nm. Green—Linear pump; Black—Left pump; Red—Right pump (b) 800 nm. Black—Linear pump; Blue—Left pump; Red—Right pump;(c) 810 nm. Blue—Linear pump;

Black—Left pump; Red—Right pump (d) 820 nm Blue—Linear pump; Black—Left pump; Red—Right pump;

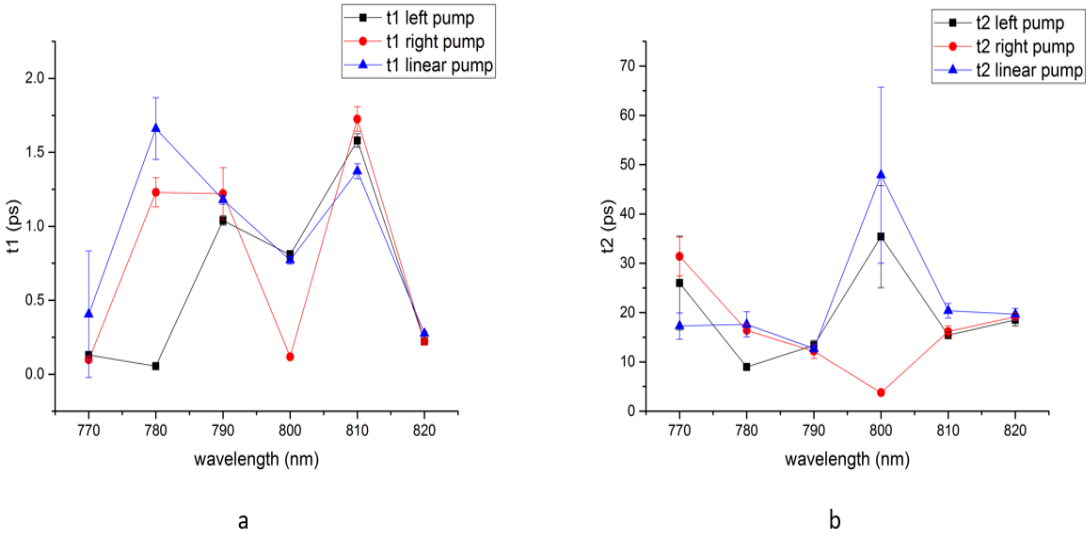

Figure 4.6 Bi-exponential decay fitting parameters. (a) Fast decay parameter time τ_1. (b) Slow decay parameter time τ_2.

All the reflectivity data is fitted by a bi-exponential decay function:

$$\Delta R = A \cdot \exp(-t/\tau_1) + B \cdot \exp(-t/\tau_2) + C \quad (4.1)$$

the fast decay τ_1 has an order of 1 ps, while the slow decay τ_2 has an order of 10 ps. The results of the decay time as a function of wavelength is shown in figure 4.6. The results of the fitting constant A, B, and C as a function of wavelength is shown in figure 4.7 The parameter A is positive for all results, however, the parameter B for 800 nm, 810 nm, and 820 nm is negative. According to previous report [14, 29], spontaneous radiation contributes to the fast decay, and phonon scatter and nonradioactive interband electron hole recombination contributes to the slow decay, and the change of τ_1 and τ_2 have no regular with the wavelengths. Unlike τ_1 and τ_2

the parameters A, B change with the pump and probe wavelengths change. The parameter A increases as the wavelengths increase, while the parameter B decreases as the wavelengths increase, and it becomes negative after 800 nm, then arrives at the lowest peak at 810 nm.

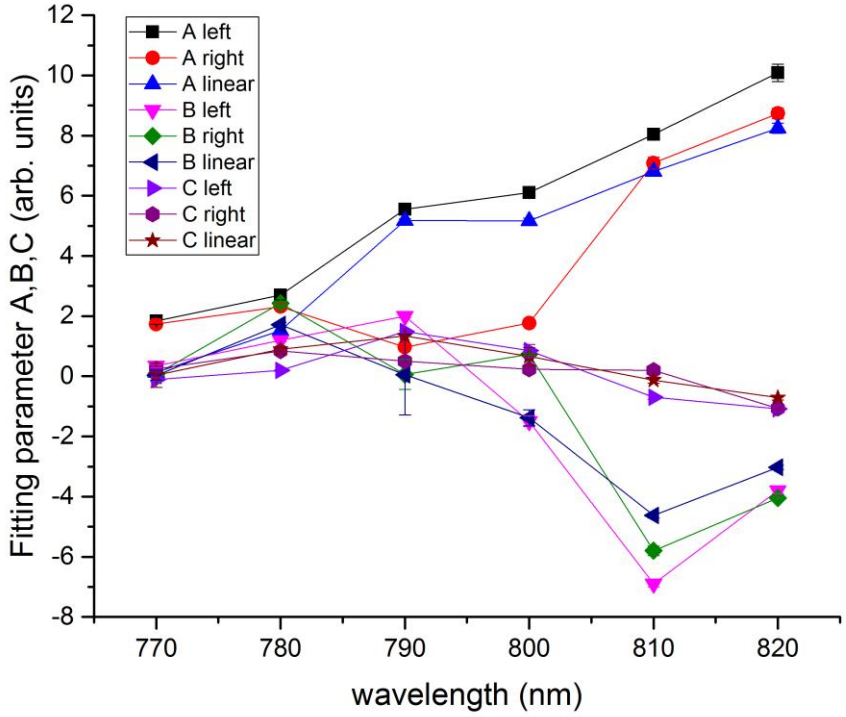

Figure 4.7 Bi-exponential decay fitting parameter A, B, and C as a function of wavelength.

Overall, the simple bi-exponential decay fitting cannot describe the whole data clearly, as we discussed before, there may be 3 or more effects have influence to the ΔR, although multi-exponential decay fittings have done, the results are much worse than bi-exponential decay fitting. One reason for this problem is the laser's pulse width

cannot be neglected. The multi-exponential decay function can be regarded as the system's reaction after being pumped by a laser pulse with a full width at half maximum (FWHM) of 250 fs, this distraction is not instantaneous when compared with the fast decay time scale. Thus, a convolution of the multi-exponential decay function and a pulse with FWHM of 250 fs is needed. The convolution function can simulate the real system reaction much better. The time-resolved Kerr rotation data is also obtained under different wavelength for the MoSe2 Kerr rotation observed in the experiment sample as shown in figure 4.8. First of all, all the experiments are done in room temperature. According to the previous studies [13, 30, 31], the spin relaxation time of TMDCs becomes extremely short when the temperature is above 120 K. Thus, the transient Kerr rotation does only exist within the first picosecond as shown in figure 4.8, which is consistent with that in the literature. For further experiments, the temperature dependence will be studied.

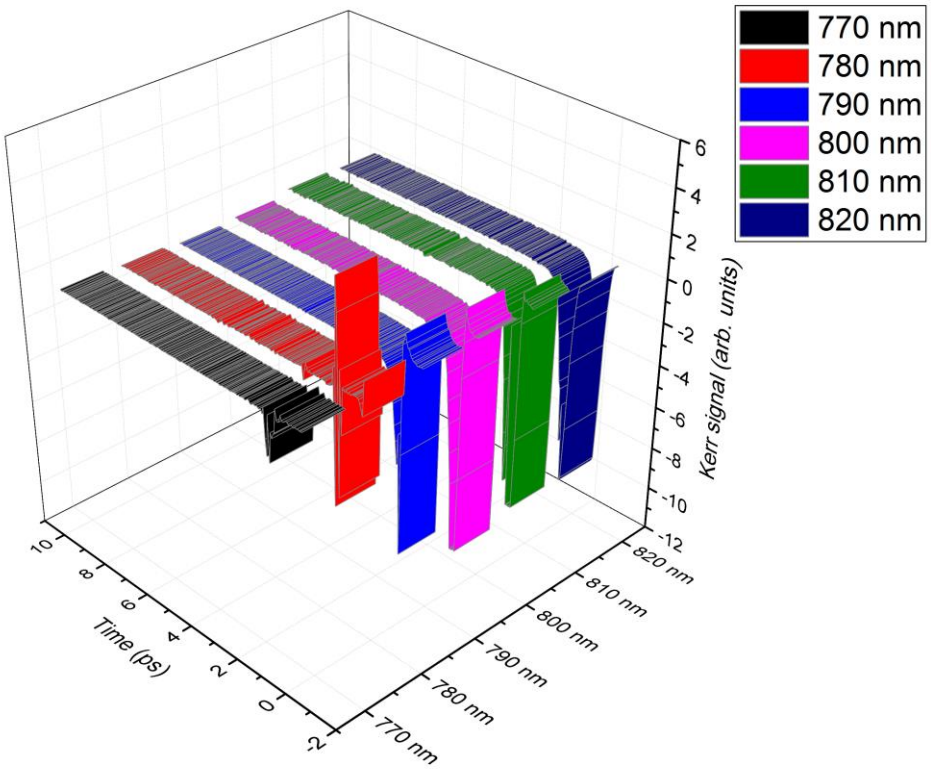

Figure 4.8 The Kerr rotation of σ^+ pump with different wavelengths.

4.3 Summary and Future work

The study of TMDCs is the most attractive topic in condense matter physics, due to its great potential application. In the last year, we have established a time-resolved optical pump-probe system to investigate the dynamic process in TMDCs. Because the time is relatively short, and the experimental setup for detecting a such small signal is much more complicated than we expected, there are still lots of works to improve

our results. I would continue the dynamic study on TMDCs and extend experiments on the following aspects.

1. Extensive wavelength dependent studies

What we can do before upgrading our experiment system is investigating the dependence between wavelengths and reflection spectrum in MoSe2. From the existing results, we know that the bandgap of MoSe2 in room temperature has a relatively great reduction. Therefore, the wavelength range would be expanded further until the threshold wavelength is reached, which will give us the information about the bandgap energy. It would also be helpful to study the wavelength dependence at a fine increment of 5 nm or less to gain more detailed band structure information.

2. A better fitting method involving convolution function

As we mentioned in chapter 4, there are at least 4 effects that impact on the pump induced reflectivity, so the fitting results of simple bi-exponential decay function are unsatisfactory. In order to obtain better fitting results, the multi-exponential decay function will be convoluted with the Gaussian pulse to simulate the real experimental condition.

3. Temperature dependant measurements

According to the previous reports, the spin relaxation time in MoS2 is long than 1 nanosecond in 5 K [13], however, this time decreases to 1 picosecond when the temperature increase to 120 K [30], and in room temperature, Kerr signal is almost negligible. Although our system can detect very weak Kerr signal at room

temperatures, a temperature dependent measurement is a must to give the spin or valley information for this material. Therefore, the cryostat will be employed in future measurements. In chapter 2, two spin relaxation mechanisms are discussed, Elliot-Yafet and Dyakonov-Perel mechanism respectively. The variable temperature measurement also helps us to define the spin relaxation mechanism in MoSe2, since the phonon scattering time is related to the temperature and these two mechanisms is related to the phonon scattering time.

4. Determine difference between degenerate measurements and non-degenerate measurements

Finally, we decide to investigate a generally but important issue, the difference between degenerate measurements and non-degenerate measurements. The energy of probe photons is an important factor to determine the revealed dynamics in the transient reflectivity/Kerr rotation data. It's important to be able to vary the probe photon energy so as to probe different position around the vicinity of the excited point. A probe with a span of spectrum around pump photon wavelength is ideal.

References

1. Kastler, A., *Optical methods of atomic orientation and of magnetic resonance.* JOSA, 1957. **47**(6): p. 460-465.
2. Dyakonov, M., *Basics of Semiconductor and spin physics*, in *Spin Physics in Semiconductors*. 2008, Springer. p. 1-28.
3. Baibich, M.N., et al., *Giant magnetoresistance of (001) Fe/(001) Cr magnetic superlattices.* Physical review letters, 1988. **61**(21): p. 2472.
4. Berger, C., et al., *Ultrathin epitaxial graphite: 2D electron gas properties and a route toward graphene-based nanoelectronics.* The Journal of Physical Chemistry B, 2004. **108**(52): p. 19912-19916.
5. Mak, K.F., et al., *Tightly bound trions in monolayer MoS2.* Nature materials, 2013. **12**(3): p. 207-211.
6. Mak, K.F., et al., *Atomically thin MoS 2: a new direct-gap semiconductor.* Physical Review Letters, 2010. **105**(13): p. 136805.
7. He, Y.-M., et al., *Single quantum emitters in monolayer semiconductors.* Nature nanotechnology, 2015. **10**(6): p. 497-502.
8. Yu, Y., et al., *Equally efficient interlayer exciton relaxation and improved absorption in epitaxial and nonepitaxial MoS2/WS2 heterostructures.* Nano letters, 2014. **15**(1): p. 486-491.
9. Woessner, A., et al., *Highly confined low-loss plasmons in graphene–boron nitride heterostructures.* Nature materials, 2015. **14**(4): p. 421-425.
10. Ulstrup, S., et al., *Ultrafast Band Structure Control of a Two-Dimensional Heterostructure.* ACS nano, 2016.
11. Parsons, R., *Band-to-band optical pumping in solids and polarized photoluminescence.* Physical Review Letters, 1969. **23**(20): p. 1152.

12. Wang, Q., et al., *Valley carrier dynamics in monolayer molybdenum disulfide from helicity-resolved ultrafast pump–probe spectroscopy.* ACS nano, 2013. **7**(12): p. 11087-11093.

13. Yang, L., et al., *Long-lived nanosecond spin relaxation and spin coherence of electrons in monolayer MoS2 and WS2.* Nature Physics, 2015.

14. Korn, T., et al., *Low-temperature photocarrier dynamics in monolayer MoS2.* Applied Physics Letters, 2011. **99**(10): p. 102109.

15. Wang, G., et al., *Valley dynamics probed through charged and neutral exciton emission in monolayer WSe 2.* Physical Review B, 2014. **90**(7): p. 075413.

16. Wang, G., et al., *Polarization and time-resolved photoluminescence spectroscopy of excitons in MoSe2 monolayers.* Applied Physics Letters, 2015. **106**(11): p. 112101.

17. Palummo, M., M. Bernardi, and J.C. Grossman, *Exciton radiative lifetimes in two-dimensional transition metal dichalcogenides.* Nano letters, 2015. **15**(5): p. 2794-2800.

18. Li, H., et al., *From bulk to monolayer MoS2: evolution of Raman scattering.* Advanced Functional Materials, 2012. **22**(7): p. 1385-1390.

19. Tonndorf, P., et al., *Photoluminescence emission and Raman response of monolayer MoS 2, MoSe 2, and WSe 2.* Optics express, 2013. **21**(4): p. 4908-4916.

20. Lee, H., et al., *RKKY interactions in graphene: Dependence on disorder and Fermi energy.* Physical Review B, 2012. **86**(20): p. 205427.

21. Zhu, Z., Y. Cheng, and U. Schwingenschlögl, *Giant spin-orbit-induced spin splitting in two-dimensional transition-metal dichalcogenide semiconductors.* Physical Review B, 2011. **84**(15): p. 153402.

22. Xiao, D., et al., *Coupled spin and valley physics in monolayers of MoS 2 and other group-VI dichalcogenides.* Physical Review Letters, 2012. **108**(19): p. 196802.

23. Žutić, I., J. Fabian, and S.D. Sarma, *Spintronics: Fundamentals and applications.* Reviews of modern physics, 2004. **76**(2): p. 323.

24. You, Y., et al., *Observation of biexcitons in monolayer WSe2.* Nature Physics, 2015. **11**(6): p. 477-481.

25. Frolov, S. and Z.V. Vardeny, *Double-modulation electro-optic sampling for pump-and-probe ultrafast correlation measurements.* Review of Scientific Instruments, 1998. **69**(3): p. 1257-1260.

26. Kimel, A., et al., *Room-temperature ultrafast carrier and spin dynamics in GaAs probed by the photoinduced magneto-optical Kerr effect.* Physical Review B, 2001. **63**(23): p. 235201.

27. Qiu, J., et al. *Helicity resolved ultrafast pump-probe spectroscopy of monolayer molybdenum disulphide*. in *SPIE Optical Engineering+ Applications*. 2014. International Society for Optics and Photonics.

28. Rivera, P., et al., *Valley-polarized exciton dynamics in a 2D semiconductor heterostructure.* Science, 2016. **351**(6274): p. 688-691.

29. Shi, H., et al., *Exciton dynamics in suspended monolayer and few-layer MoS2 2D crystals.* ACS nano, 2013. **7**(2): p. 1072-1080.

30. Zhu, C., et al., *Exciton valley dynamics probed by Kerr rotation in WSe 2 monolayers.* Physical Review B, 2014. **90**(16): p. 161302.

31. Yan, T., et al., *Exciton valley dynamics in monolayer WSe2 probed by the two-color ultrafast Kerr rotation.* Physical Chemistry Chemical Physics, 2016.